

Dissipative self-assembly of patchy particles under nonequilibrium drive: a computational study

Shubhadeep Nag[†] and Gili Bisker^{*,†,‡,¶,§,||}

[†]*Department of Biomedical Engineering, Faculty of Engineering, Tel Aviv University, Tel Aviv 69978, Israel*

[‡]*The Center for Physics and Chemistry of Living Systems, Tel Aviv University, Tel Aviv 6997801, Israel*

[¶]*The Center for Nanoscience and Nanotechnology, Tel Aviv University, Tel Aviv 6997801, Israel*

[§]*The Center for Light-Matter Interaction, Tel Aviv University, Tel Aviv 6997801, Israel*

^{||}*The Center for Computational Molecular and Materials Science, Tel Aviv University, Tel Aviv 6997801, Israel*

E-mail: bisker@tauex.tau.ac.il

Abstract

Inspired by biology and implemented using nanotechnology, the self-assembly of patchy particles has emerged as a pivotal mechanism for constructing complex structures that mimic natural systems with diverse functionalities. Here, we explore the dissipative self-assembly of patchy particles under nonequilibrium conditions, with the aim of overcoming the constraints imposed by equilibrium assembly. Utilizing extensive Monte Carlo (MC) and Molecular Dynamics (MD) simulations, we provide insight into

the effects of external forces that mirror natural and chemical processes on the assembly rates and the stability of the resulting assemblies comprising 8, 10, and 13 patchy particles. Implemented by a favorable bond-promoting drive in MC or a pulsed square wave potential in MD, our simulations reveal the role these external drives play in accelerating assembly kinetics and enhancing structural stability, evidenced by a decrease in the time to first assembly and an increase in the duration the system remains in an assembled state. Through the analysis of an order parameter, entropy production, bond dynamics, and interparticle forces, we unravel the underlying mechanisms driving these advancements. We also validated our key findings by simulating a larger system of 100 patchy particles. Our comprehensive results not only shed light on the impact of external stimuli on self-assembly processes but also open a promising pathway for expanding the application by leveraging patchy particles for novel nanostructures.

1 Introduction

Self-assembly is a fundamental process in nature, in which particles within a bounded system spontaneously organize into an ordered structure, directed by intermolecular interactions. This phenomenon is not only pivotal in a myriad of biological processes, such as protein folding and cell membrane formation, but it also plays a crucial role in advancing nanotechnology, facilitating the creation of sophisticated structures across multiple scales.¹⁻⁷ Particularly in nanoscience, self-assembly enables the development of innovative applications, ranging from drug delivery systems, exemplified by liposomes formed from lipid bilayers,⁸⁻¹⁰ to the construction of advanced materials for photonic and electronic sensing devices using organized gold nanoparticles.¹¹⁻¹³ These diverse applications accentuate the importance of understanding and modeling self-assembly processes.

Self-assembly is categorized into two primary types: static and dissipative. In static self-assembly, the formed structure does not rely on any external source of energy to maintain itself, and the system minimizes its free energy under equilibrium conditions.¹ Conversely,

dissipative self-assembly occurs under nonequilibrium conditions, often at the expense of external energy sources, and the system dissipates energy to maintain its structure.¹⁴⁻¹⁷ This nonequilibrium behavior is driven by a continuous energy supply from various sources such as light,¹⁸ chemical fuels,^{19,20} electric,²¹ and magnetic fields,²² resulting in a non-zero difference between the forward and backward fluxes, thereby activating individual components and form the desired structures.

The theory of dissipative states, first introduced by Prigogine,²³ is continuously developing and is found to be relevant to many biological phenomena.^{15,24-28} Particularly, the thermodynamics of continuous energy-driven structure forming systems in nonequilibrium conditions has been a rapidly developing field with the introduction of various design principles to model dissipative self-assembly.²⁹⁻³⁵ One major goal of these studies is to overcome the bottlenecks or trade-offs imposed by equilibrium or static self-assemblies.

Equilibrium self-assembly raises many unavoidable trade-offs, each reflecting the intricate balance systems must achieve. For example, a system might navigate a trade-off between kinetic and thermodynamic factors, such that it may become confined in kinetically trapped states, failing to achieve the most thermodynamically favorable configuration. This can result in suboptimal or inefficient assembly processes.²⁵ Numerous design principles have been suggested to overcome kinetically trapped states.^{36,37} To circumvent these limitations, researchers have explored diverse self-assembly strategies, employing nonreciprocal interactions and driving systems from arrested dynamics towards lower-energy configurations.^{38,39} This strategy leverages nonequilibrium dynamics and programmable interactions, opening up new avenues for the creation of dynamic, self-organizing structures across different scales - from nucleic acids to colloidal particles, facilitating automated control over structural transitions in living systems.⁴⁰ Additionally, Boekhoven and colleagues introduced a dissipative self-assembling system that utilizes external fuel, analyzing the associated entropy production and lost work.^{41,42} England explored the complex thermodynamics of nonequilibrium processes, crucial in understanding self-assembly and self-replication in biological systems.²⁸

His work delves into the challenges of modeling nonequilibrium scenarios, especially in driven self-assembly, proposing mechanisms for self-organization via energy dissipation.^{15,43,44}

Biological systems also exhibit these two types of assemblies. For instance, static self-assembly orchestrates the formation of functional hemoglobin proteins from hemoglobin polypeptides and functional ribosomes from the combination of RNA and ribosomal proteins.⁴⁵ In contrast, dissipative self-assembly plays a crucial role in cell division and macromolecular assembly, such as tubulin dimer organization into microtubules facilitated by Guanosine triphosphate (GTP) hydrolysis, and chaperone-mediated macromolecule formation through Adenosine triphosphate (ATP) hydrolysis.⁴⁶⁻⁴⁹ Additionally, it is integral to active matter, driving self-organization in cellular cytoskeletons and bacterial colonies using external energy sources.⁵⁰ Furthermore, experimental studies have highlighted the importance of ATP and GTP induced self-assembly systems,^{51,52} offering profound insights into the development of synthetic cells, prebiotic systems, and nanosystems.^{53,54} These advancements enhance our understanding of dissipative self-assembly modeling, crucial for deepening our comprehension of biological structures and offering significant potential in biochemical and materials sciences.⁵⁵⁻⁵⁷

The aforementioned example of the organization of tubulin dimers into microtubules, facilitated by GTP hydrolysis, serves as a primary example of dissipative self-assembly found in our cell.⁴⁷ These microtubules feature a cylindrical shape with a hollow core, appearing as a ring of 13 dimers when viewed perpendicularly to the core's radius.⁵⁸ Similar ring-like self-assembly structures are found in circular DNA and cyclic protein complexes, which are crucial for understanding complex biological assembly processes.⁵⁹⁻⁶¹ The significance of these rings extends into nanoscience, serving as foundational blueprints for developing self-assembled nanorings.^{62,63} These nanorings, far from being merely minuscule structures, are pivotal building blocks for transformative applications in drug delivery, nanoelectronics, and photonic devices.⁶⁴ Therefore, modeling such ring-like structures, and utilizing the external sources of energy helps understand biological phenomena and design advanced materials.

Computational studies play a crucial role in advancing our understanding of structures created through dissipative self-assembly, offering deeper microscopic insights. Within this framework, patchy particles, characterized by distinct patches that enable selective, anisotropic binding, emerge as a fundamental model system.⁶⁵ The theoretical foundation for these interactions traces back to seminal theories proposed by Boltzmann,⁶⁶ and were first practically demonstrated with the synthesis of Janus particles, a notable subclass of patchy particles, in the late 1980s.⁶⁷ The specific term ‘patchy particle’ was later formally coined,⁶⁸ and the introduction of this concept has unlocked vast possibilities in predicting crystal structures, thereby significantly contributing to the advancement of nanoscience and nanofabrication. This breakthrough has sparked a wave of research, exploring the broad applications and potential of patchy particles in various domains.^{69–74} For example, Gong *et. al.* synthesized patchy particles using colloidal fusion.⁷¹ Additional study demonstrated the synthesis of Janus particles using evaporative deposition of preferential materials on spheroid, changing the properties of one hemispheroid.⁷⁵ Chang and others showed a simple yet effective technique by using seed-mediated heterogeneous nucleation to synthesize patchy particles.⁷⁶ These patchy particles have been found useful in many potential applications such as targeted drug delivery,^{77,78} photonic crystals,^{79–82} phoretic motors,⁸³ and more. Recent explorations into the self-assembly of patchy particles under external stimuli, such as electric⁸⁴ and magnetic fields,⁸⁵ have further highlighted their role in advancing new material designs.

In computational research, patchy particles have been extensively employed to simulate diverse systems, such as protein droplets^{86,87} and colloidal assemblies,⁶⁵ enabling a profound exploration of phenomena like crystal nucleation and growth,^{88,89} liquid-liquid phase transitions,⁸⁶ and protein folding,⁹⁰ among others.^{91–93} By tuning the characteristics of patches, models based on patchy particles have offered insights into the phase behavior of colloids.⁹⁴ Specifically, Nguemaha *et. al.* utilized Monte Carlo (MC) simulations with two-component patchy particles to investigate RNA’s role in the liquid-liquid phase separation observed

within membrane-less organelles, focusing on protein mixtures that incorporate regulatory components.⁸⁶ Similarly, Gnan, Sciortino, and Zaccarelli’s coarse-grain modeling of proteins using patchy particles has shed light on protein phase behavior.⁸⁷ Espinosa *et. al.* have also contributed by employing Molecular Dynamics (MD) simulations with patchy particles to demonstrate deviations from the law of rectilinear diameter through an examination of liquid-vapor coexistence phase behavior.⁹⁵ Thus, the well-established understanding of patchy particles positions them as an ideal model system, which aims to leverage these insights further to understand biological self-assembly phenomena and pioneer new materials.

Designing such new materials requires the mitigation of the aforementioned trade-offs effectively. One unique approach to achieve this is by driving the system into non-equilibrium conditions, for example, through the introduction of a self-healing driving force.⁹⁶ This proposed model of dissipative self-assembly is based on information from equilibrium self-assembly and biological processes such as the use of chemical fuel to organize structures with specific functions similar to the way microtubules are formed by α -tubulin and β -tubulin through GTPase activity.⁹⁷ Inspired by these processes, it was demonstrated that nonequilibrium driving enhances dimer-based self-assembly, enabling smaller critical seeds and improved stability of target structures compared to equilibrium scenarios.⁹⁸ Using a similar model, the stochastic landscape method was proposed for improving the predictive power for first assembly times, offering a quantitative framework for understanding and controlling nonequilibrium self-assembly processes.⁹⁹ Recently, it has been used to classify protein states.¹⁰⁰

In the present study, we aim to expand this approach of nonequilibrium driving force by undertaking a detailed exploration of self-assembly mechanisms using patchy particles in three-dimension (3D), employing a comprehensive simulation approach. Our investigation begins with equilibrium MC simulations across three distinct systems, each comprising 8, 10, and 13 patchy particles, respectively, where each particle has two possible internal states. These particles are specifically designed to achieve target structures of n -sided polygons or

n -ring configurations, comprising all the particles in the system. We examine the formation dynamics and stability of the self-assembled structures, particularly in relation to the varying interaction energies between patches, and identify a domain of equilibrium trade-offs, delineating a complex relationship between assembly time and structural stability. To overcome these trade-offs, an external bias is introduced, shifting the dynamics to the nonequilibrium regime, inspired by biological systems that exploit energy molecules like ATP and GTP thus mimicking the continuous energy supply essential for sustaining assembly processes in living systems.¹⁰¹ A rigorous thermodynamic analysis encompassing entropy production and total energy computations shows how this externally applied drive enables the system to form the target structure faster compared to the equilibrium case. Complementing the MC results, we perform MD simulations for systems of 8 and 10 patchy particles under both equilibrium and nonequilibrium conditions. For nonequilibrium MD simulations, a square wave potential is applied periodically as an external drive, where we further analyze the bond formation and breakage statistics, the underlying forces, and an order parameter to distill the underlying mechanism governing the dissipative self-assembly. We demonstrate how the oscillating potential induces momentary forces that accelerate the assembly, allowing the system to rapidly achieve the target structure. By revealing the nuanced dynamics of dissipative self-assembly with patchy particles, this study highlights the critical role of external energy in guiding assembly processes. Our insights offer a foundation for novel approaches in biophysics and material engineering, setting the stage for advancements in the design and control of self-assembling systems.

2 Computational Framework

2.1 Simulation Cells

MC simulations were conducted for three systems, comprising 8, 10, and 13 patchy particles, whereas MD simulations were conducted for systems with 8 and 10 patchy particles. Each

particle was designed with two surface patches and varied states depending on the system. In the systems with 8 and 10 patchy particles, we divided the particles into two distinct states, labeled α and β , with equal distribution among the particle populations. Conversely, in the system comprising 13 patchy particles, we introduced a third state, γ , alongside the existing α and β states. In this scenario, six particles were assigned to the α state and another six to the β state, with the remaining particle embodying the γ state. Our objective was to form target structures that emulate polygons with 8, 10, and 13 sides, corresponding to each system (Fig. 1). To realize these structures, the patches on each particle were meticulously positioned to ensure that the angle between two lines - each extending from a patch to the particle's center - matched the interior angles of an 8-sided, 10-sided, and 13-sided polygon, respective to each system. These angles are 2.356 rad, 2.513 rad, and 2.658 rad for 8, 10, and 13 patchy particle system respectively. Furthermore, the size of the cubic simulation boxes was carefully chosen based on the number of patchy particles to be 8 Å, 9 Å, and 15 Å for the 8-particle, 10-particle, and 13-particle systems, respectively. In MD simulation, we simulated 8 and 10 particle systems with the same simulation parameters as described above, except that the particles had only one internal state, α .

2.2 Interaction Potential of Patchy Particles

Patchy particle simulations have been a versatile tool for modeling a wide range of structures, ranging from proteins and DNA to small molecules and atoms.¹⁰² Kern and Frenkel proposed an approach for simulating patchy particles by modeling the bead of the patchy particles with hard-sphere potential and patches with both square well potential along with an angular dependent potential.¹⁰³ This model has been shown effective in simulating many cases of patchy particles.^{88,104–107}

We build upon the Kern-Frenkel approach and apply it to our system of 8, 10, and 13 patchy particles. Based on this approach, each patchy particle is featured with patches of an angular width of $2\theta^{max}$ centered to the core of the bead and length $\delta/2$ (Fig. 2(a)). In

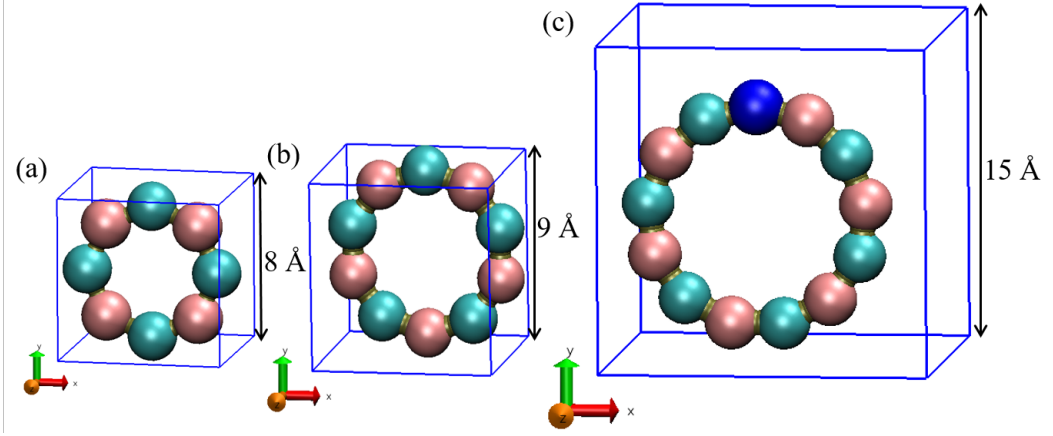


Figure 1: Target structures of (a) 8-patchy particle system, (b) 10-patchy particle system, and (c) 13-patchy particle system. Each target structure is presented within its cubic simulation cell, with lattice parameters set to 8 Å, 9 Å, and 15 Å for the 8, 10, and 13-particle systems. In the 8 and 10-particle systems, particles in states α and β are represented by pink and cyan colors, respectively. For the 13-patchy particle system, the γ state appears in blue.

this framework, the total interaction energy of a patchy particle, $U_{Particle}$, is:

$$U_{Particle} = U_{bead} + U_{patch} \quad (1)$$

where U_{bead} and U_{patch} are the energies associated with the bead and the patch, respectively.

The expression of U_{bead} is modeled as Lennard-Jones (LJ) interaction:

$$U_{bead} = \begin{cases} 4\epsilon_{bead} \left[\left(\frac{\sigma_{bead}}{r_{ij}} \right)^{12} - \left(\frac{\sigma_{bead}}{r_{ij}} \right)^6 \right], & \text{if } \sigma_{bead} < r_{ij} < r_c \\ 0, & \text{otherwise} \end{cases} \quad (2)$$

where ϵ_{bead} is the depth of the potential well of the bead and σ_{bead} is its van der Waals (vdW) radius. These two values are set at 0.75 kJ/mol and 2 Å throughout the simulation. When the distance between two patchy particles i and j , denoted as r_{ij} , is smaller than the cut-off distance, r_c , the particles interact. Here, r_c is taken as 5 Å.

In the case of MC simulation of 8 and 10 patchy particles, the two different states α and β attract each other, whereas the same states do not interact with each other ($U_{patch}^{\alpha\alpha} =$

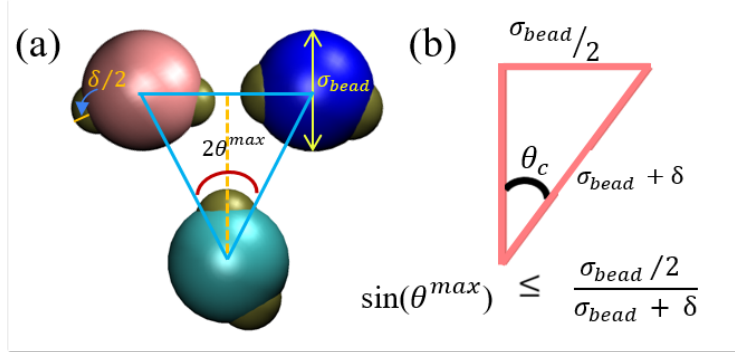


Figure 2: Patchy particles model. (a) A schematic where three patchy particles may potentially interact with each other, resulting in an unwanted case of multiple bonds per patch. (b) A specific condition is implemented to prevent more than a single bond per patch (see details in the main text). This figure is a schematic representation created to visualize the concepts described, with dimensions and proportions aligned with those used in our simulations.

$0, U_{patch}^{\beta\beta} = 0$). The patch energy $U_{patch}^{\alpha\beta}$ between α and β states of the 8 and 10 patchy particle systems is:

$$U_{patch}^{\alpha\beta} = \epsilon_{patch} \sum_{\alpha, \beta=1}^2 f(\vec{r}_{ij}, \hat{n}_i^\alpha, \hat{n}_j^\beta), \quad \text{if } \sigma_{bead} < r_{ij} < \sigma_{bead} + \delta \quad (3)$$

where ϵ_{patch} denotes the depth of the potential between patches of the particle, \vec{r}_{ij} is the vector connecting the center of particle i^{th} to the center of particle j^{th} , \hat{n}_i^α or \hat{n}_j^β denote the unit vector connecting the center of the bead and the center of patches of the patchy particle of state α or β , respectively, and $f(\vec{r}_{ij}, \hat{n}_i^\alpha, \hat{n}_j^\beta)$ is the angular dependence in the interaction between patches, and which is given by:

$$f(\vec{r}_{ij}, \hat{n}_i^\alpha, \hat{n}_j^\beta) = \begin{cases} 1, & \text{if } \vec{r}_{ij} \cdot \hat{n}_j^\alpha > \cos(\theta^{max}) \text{ \& } \vec{r}_{ji} \cdot \hat{n}_j^\beta > \cos(\theta^{max}) \\ 0, & \text{otherwise} \end{cases} \quad (4)$$

This condition ensures that the patchy interaction potential is activated only when the angle between \vec{r}_{ij} , and the unit vectors \hat{n}_i^α and \hat{n}_j^β , representing the orientation of their respective patches, falls within half of the angular width of the patch, θ^{max} . Specifically, this occurs when both $\vec{r}_{ij} \cdot \hat{n}_i^\alpha$ and $\vec{r}_{ij} \cdot \hat{n}_j^\beta$ are larger than the cosine of θ^{max} . When these conditions are

satisfied, meaning the patches are correctly aligned, the angular dependency term equals 1, and the interaction potential U_{patch} of Eq. 1 contributes to the total interaction energy of the patchy particle.

For the 13 patchy particles system, there are three internal states: α , β , and γ . The α and β states interact with each other similar to the 8 and 10 particle cases. The interaction between the γ state and the α or β states is the energy $U_{patch}^{\alpha/\beta\gamma}$, with a similar form as Eq. 3 and the corresponding angular dependence $f(\vec{r}_{ij}, \hat{n}_i^{\alpha/\beta}, \hat{n}_j^\gamma)$ similar to Eq. 4. This ensures that the interaction potential U_{patch} is activated only when both the angle between \vec{r}_{ij} and the unit vector $\hat{n}_i^{\alpha/\beta}$, and the angle between \vec{r}_{ji} and \hat{n}_j^γ , fall within half of the angular width of the patch, θ^{max} . Here, \hat{n}_j^γ denotes the unit vector connecting the center of the bead and the center of patches of the γ patchy particle.

To ensure a single bond per patch,^{102,108} the length of the patch must be related to the angular width by the inequality $\sin(\theta^{max}) \leq (\sigma_{bead}/2)/(\sigma_{bead} + \delta)$. To satisfy this condition, we chose θ^{max} to be 0.35 radians. The schematic of this condition is shown in Fig. 2(b).

2.3 Initial Conditions

To rigorously assess the inherent trade-offs associated with equilibrium simulations and to determine how an external bias can mitigate these limitations, our investigation centers on two critical metrics, namely, the time until the first self-assembly event, T_{fas} , and time the system remains in the assembled state as a proxy for target stability, T_{stable} . Accordingly, our approach in both MC and MD simulations encompassed two distinct methodologies in which the initial conditions were set to be random, for analyzing T_{fas} , or as the target structure, for analyzing T_{stable} . In the former, the simulation was initiated with patchy particles distributed randomly in the simulation box, designed to meticulously observe and record the time frame leading to the first emergence of the target structure. In the latter case, the simulation was initiated with a pre-formed target structure to diligently monitor and analyze the enduring stability and structural integrity of the assembly. Using these

two different initial conditions, we aimed to acquire a comprehensive understanding of the dynamics and robustness of the structures formed under equilibrium and nonequilibrium conditions. Throughout our study, we presented the median values of T_{fas} and T_{stable} , and showed the full distribution of the assembly and disassembly times whenever possible. The rationale is attributed to the fact that in order to compute the mean, we must consider realizations in which the systems successfully assemble for T_{fas} or disassemble for T_{stable} . These would be highly computationally expensive, particularly for lower interaction energies and very high interaction energies, respectively.

2.4 Monte Carlo Simulation

Our in-house program of patchy particles included both equilibrium and nonequilibrium MC simulations. The MC moves comprised both the translation of the beads and the rotation of patches relative to the center of the bead. All the MC simulations in this work were performed at a temperature of 65 K, and we have employed reflective walls. The simulation lengths, in terms of the number of MC steps, were set to 10×10^6 for realizations starting from both random and target configurations to determine T_{fas} and T_{stable} for the 8 and 10 patchy particle systems. For the 13-patchy particle system, given its increased complexity and the intricate nature of the target structure, the number of MC steps was increased to 15×10^6 to adequately capture the assembly process and ensure the formation of the target structure.

2.4.1 Equilibrium Simulations

In equilibrium MC simulation, each step involved assessing the total interaction energy of the particles, both before and after a proposed MC step. We then employed the Metropolis criterion,¹⁰⁹ which provided the probability for accepting or rejecting a move, according to the energy difference, $\min\left[1, \exp\left\{-\left(U_{Particle}^{new} - U_{Particle}^{old}\right)/k_B T\right\}\right]$, where $U_{Particle}^{new}$ and $U_{Particle}^{old}$ represent the new and old total energies, k_B is the Boltzmann constant and T is the

temperature.

2.4.2 Nonequilibrium Simulations

In our nonequilibrium MC simulation, we introduced an external driving force, denoted as ϵ_{drive} , to the patches of the particles. This external force disrupted the equilibrium state of the system by deviating from the detailed balance condition, significantly changing the interaction dynamics between the particles. We applied this bias in a targeted manner, depending on whether the patches were moving towards or away from each other, aligning with the topology of the desired target structure to both form and maintain it.

The acceptance or rejection of a proposed move was adjusted to include the drive. If two patches of two different patchy particles, which were the nearest neighbor of each other in the target structure, came into proximity in an MC step, the drive would render the proposed move more favorable by modifying the acceptance probability to $\min[1, \exp\{- (U_{Particle}^{new} - \epsilon_{drive} - U_{Particle}^{old})/k_B T\}]$. When two neighboring patches, which are adjacent in the target structure, move apart during an MC step, the drive would render the bond breaking less probable, by the modified acceptance probability to $\min[1, \exp\{- (U_{Particle}^{new} + \epsilon_{drive} - U_{Particle}^{old})/k_B T\}]$. When a virtual bond between two nearest neighbor patches, according to the target structure, persisted over successive MC steps, no external bias was added nor subtracted, and the acceptance probability followed the traditional Metropolis algorithm. The application of an external driving force (ϵ_{drive}) in nonequilibrium simulations is hypothesized to significantly enhance the efficiency of target structure formation and its subsequent stability, by selectively favoring assembly pathways that align with the desired target structure.

Our approach of external drive replicates the directed self-assembly processes found in experimental systems like DNA nanostructures and colloidal crystals.^{110–113} In these experiments, specific interactions and external stimuli, such as light, pH variations, and electromagnetic fields, guide the formation of the desired structures. For instance, light and pH

control in DNA assembly and disassembly enables DNA structures to adapt to various stimuli, exhibiting properties necessary for synthetic cells.¹¹⁰⁻¹¹² Similarly, applying magnetic fields in colloidal crystal assembly selectively stabilizes favorable configurations by adjusting energy levels.¹¹³ These experimental analogs ensure that our simulations are grounded in realistic and practically achievable conditions.

Complementary to the 8, 10, and 13 patchy particle simulations aimed to understand the formation and stability of the target structures, comparative analyses were conducted to assess the effects of patch length variation and simulation cell dimension variation. These were carried out in 10 patchy particle systems to achieve insights into the factors influencing the self-assembly.

2.5 Molecular Dynamics Simulations

2.5.1 Equilibrium Simulations

Equilibrium MD simulations were conducted using the Large-scale Atomic/Molecular Massively Parallel Simulator (LAMMPS) software¹¹⁴ within the canonical ensemble. We focused on two specific systems comprising 8 and 10-patchy particles, each featuring only a single internal state. Consistent with the MC simulations, the dimensions of the simulation cell for these systems were maintained at 8 and 9 Å, respectively, and periodic boundary conditions (PBC) were employed in all directions. The target structure for these simulations, depicted in Figs. 1(a) and (b), maintained uniform colors for all beads across both systems according to the single state particles.

Following the study of Jover *et. al.*, the bead of the patchy particle is modeled with pseudo-hard-sphere (PHS) potential:¹¹⁵

$$U_{bead} = \begin{cases} \lambda_r \left(\frac{\lambda_r}{\lambda_a}\right)^{\lambda_a} \epsilon_r \left[\left(\frac{\sigma_{bead}}{r}\right)^{\lambda_r} - \left(\frac{\sigma_{bead}}{r}\right)^{\lambda_a} \right] + \epsilon_r, & \text{if } r < \left(\frac{\lambda_r}{\lambda_a}\right) \sigma_{bead} \\ 0, & \text{if } r \geq \left(\frac{\lambda_r}{\lambda_a}\right) \sigma_{bead} \end{cases} \quad (5)$$

where $\lambda_a = 49$ and $\lambda_r = 50$ are the coefficients for attractive and repulsive forces, respectively. The parameter ϵ_r represents the interaction strength in the PHS model, characterizing the energy associated with the interactions. The variable r signifies the distance measured from the center of one particle to another. Further, the values for ϵ_r and σ_{bead} are set to be 0.24 kJ/mol and 2 Å, respectively, aligned with the parameters utilized by Espinosa *et al.* in their investigation of liquid-vapor coexistence in systems comprising patchy particles.⁹⁵ These parameters have been established to provide a realistic representation of particle interactions within the simulated environment.

The interaction energy between patches of different particles, $U_{\text{patch}}^{\text{csw}}$, is modeled with a continuous attractive square-well potential:¹¹⁶

$$U_{\text{patch}}^{\text{csw}} = -\frac{1}{2}\epsilon_{\text{patch}} \left[1 - \tanh\left(\frac{r - r_w}{\eta}\right) \right] \quad (6)$$

where r refers to the distance between the centers of two patches on different particles, r_w is the radius of the attractive well, while the steepness of the well is controlled by η . In this context, r_w is equivalent to the width of the patches previously introduced in the simulation. In MD simulations, we have chosen the masses of the interaction sites to be 10% of the mass of the bead particle. The specific values of the core particle and patch were taken as 10 amu and 1 amu. However, the choice of masses might affect the quantitative nature but does not affect the qualitative nature of the key findings of our study since our external drive protocol does not depend on inertia. To ensure that only one bond forms per patch, we have set the values of η and r_w to be $0.005\sigma_{\text{bead}}$ and $0.12\sigma_{\text{bead}}$ respectively.

MD simulations were performed at a temperature of 40 K using the Nose-Hoover thermostat,^{117,118} which is lower compared to the 65 K set in MC, to minimize fluctuations in the system. Nevertheless, employing two different temperatures does not affect our conclusions, as the system dynamics inherently depend on the ratio of ϵ_{patch} to $k_B T$. The simulation duration for studying the self-assembly formation from both random initial conditions and

starting at the target configuration was set to 12000 ps. We integrated the equation of motion using the velocity Verlet algorithm¹¹⁹ with a carefully selected timestep of 0.2 fs, chosen to ensure the stability and non-divergence of the simulations. During these simulations, we recorded the trajectories and total interaction energy between patches every 100 fs.

2.5.2 Nonequilibrium Simulations

In our nonequilibrium MD simulations using LAMMPS, we have integrated an external drive of a square wave potential $U_{square}(t)$. Drawing inspiration from various biological systems, such a drive resembles the voltage-gated ion channels found in neurons that open and close in response to voltage changes,¹²⁰ allowing for quick transmission of electrical signals. It is also similar to the bistable genetic switches that enable cellular phase transitions under specific conditions.¹²¹ Recent experimental studies, such as the one conducted by Song *et al.*⁸⁴ and the capability of electromagnetic fields to direct the assembly of non-spherical particles studied by Shields *et al.*,⁸⁵ further support our approach.

To simulate the influence of an external periodic drive, a square wave potential, $U_{square}(t)$, is employed to modulate patchy particle interactions within the LAMMPS framework,¹¹⁴ defined as:

$$U_{square}(t) = \begin{cases} U_{high}, & 0 \leq t < \frac{T}{2} \\ U_{low}, & \frac{T}{2} \leq t < T \end{cases} \quad (7)$$

where U_{high} and U_{low} correspond to the high energy and low energy amplitudes, and T is the period of the oscillation. This approach simulates the effect of an external drive by periodically shifting the interaction energy between the patchy particles, thus driving the system away from equilibrium.

By adding the square wave potential to the base patchy interaction potential, U_{patch}^{csw} in Eq. 6, we introduce a time-dependent interaction potential that oscillates between two defined energy states. These states, corresponding to the high and low energy phases of the square wave, simulate the presence of an external driving force acting on the particles (see

Eqs. 11 and 12 of the main manuscript). This method provides a computationally feasible technique to study the dynamic self-assembly processes under nonequilibrium conditions.

The interaction potential between two patchy particles now includes two types of terms, a spatial-dependent term, $U_{patch}^{csw}(r)$, and a time-dependent term, $U_{square}(t)$ (see Eq. 7). The new modified interaction potential, $U_{patch}^{mod}(r, t)$, is given by:

$$U_{patch}^{mod}(r, t) = U_{patch}^{csw}(r) + U_{square}(t) \quad (8)$$

and the modified total interaction energy of a patchy particle is:

$$U_{particle}^{mod}(r, t) = U_{bead}(r) + U_{patch}^{mod}(r, t) \quad (9)$$

where $U_{patch}^{mod}(r, t)$ oscillates around the intrinsic patchy interaction potential, $U_{patch}^{csw}(r)$. This oscillation introduces nonequilibrium conditions by periodically altering the interaction landscape.

Fig. 3 provides a visual representation of the square wave potential modulation of the interaction potential between patchy particles for baseline interaction energy of 5 kJ/mol (Fig. 3(a)), and 6 kJ/mol (Fig. 3(b)), with their respective high and low energy phases and an external wave potential amplitude of 20 kJ/mol.

The period of the square wave, set to 20 ps, ensures a rapid effect relative to the bond formation timescale, with amplitude variations directly mimicking the external drive adjustments in the nonequilibrium MC simulations. These settings allow us to explore the dynamics of self-assembly and structural stability under nonequilibrium conditions through T_{fas} and T_{stable} . Excluding the periodic square potential, the rest of the simulation details, including the time-step, frequency of storing trajectories, and boundary conditions, were similar to the case of the MD simulation under equilibrium conditions.

In both MC and MD simulation, all the values of T_{fas} and T_{stable} were obtained from 20 distinct simulations for a given ϵ_{patch} and ϵ_{drive} values. Randomization of the 20 MC

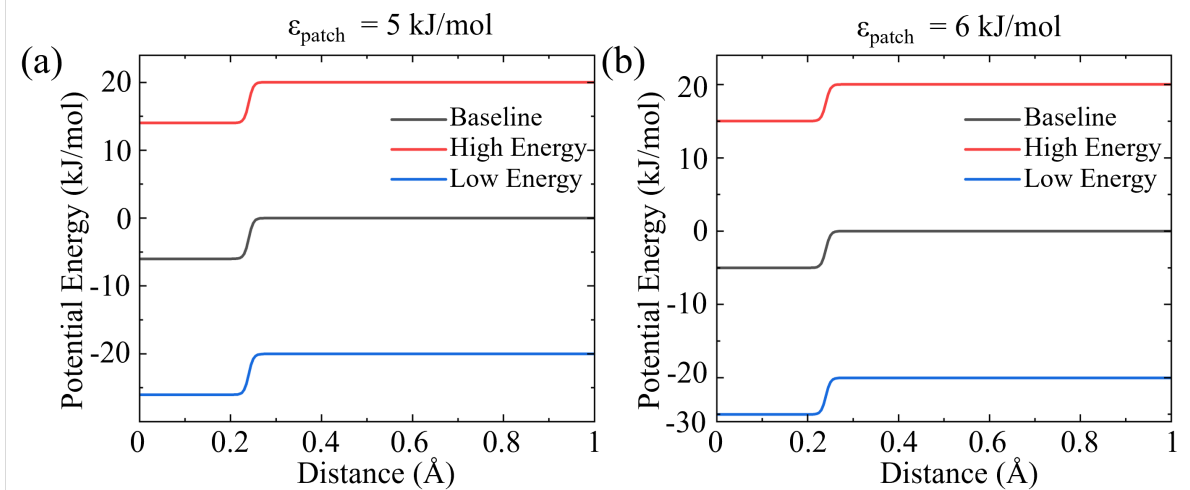


Figure 3: Patchy interaction potential, ϵ_{patch} , having a baseline value (black) of (a) 5 kJ/mol and (b) 6 kJ/mol, and the corresponding high energy (red) and low energy (blue) phases of the square wave potential with a potential of 20 kJ/mol.

simulations stems from the different values of the random seed generator, whereas for MD simulations, randomization stems from different velocity distributions from the random seed generator.

We also simulate both MC and MD for a larger system comprising 100 particles in a simulation box with dimensions of $30 \times 30 \times 30 \text{ \AA}^3$, maintaining a number density of 0.003 \AA^{-3} . This is consistent with our previous simulation of 13 patchy particles in a cubic box with a side length of 15 \AA , using a single interaction state between the patches. The simulation cell walls are modeled with PBC. The duration of the MC simulations is 5×10^6 MC steps, and the MD simulation is 10 ns. During the simulation, we maintain a neighbor list with a cutoff distance of 10 \AA , updating this list every 10 MC steps for MC simulation and 2 fs for MD simulation. The particles interact with each other through PHS potential (Eq. 5), and patches are modeled with angles set to match an 8-ring structure and a 4-ring structure while keeping other parameters identical to those used in the smaller-scale systems. For this large system, both MC and MD simulations were carried out at 40 K.

3 Results and Discussion

3.1 Monte Carlo Simulation Results

In our study, we begin by conducting equilibrium Monte Carlo simulations for three different types of systems. The first two systems consist of 8 and 10 patchy particles with two internal states denoted by α and β . The third system consists of 13 patchy particles with three internal states denoted by α , β , and γ . Each realization is initiated at random configuration, aiming to self-assemble into the desired polygonal ring structure respective to its particle count. The assembly process is documented in snapshots (Fig. 4), from the initial disorder to the final ordered state.

For the 8-particle system (Fig. 4(a)), snapshots at initial, intermediate (0.04×10^6 and 0.12×10^6 MC steps), and final stages (0.23×10^6 MC steps) illustrate a straightforward path to the target structure, indicating a simple energy landscape conducive to rapid assembly. The 10-particle system (Fig. 4(b)) showcases a more gradual formation process. Initial and subsequent snapshots taken at 0.19×10^6 , 0.79×10^6 , and 1.08×10^6 MC steps reveal an extended assembly time influenced by the larger particle count, underscoring the scaling challenges in self-assembly processes. The assembly of a 13-particle system (Fig. 4(c)) is the most intricate, achieving the target state at 3.34×10^6 MC steps after navigating through various stages. These snapshots collectively display the inherent complexity of each system and exemplify the typical pathway to the target configuration.

These configurations, captured at different MC steps and conducted under an interaction energy of 10 kJ/mol, highlight the kinetic pathways and the balance between entropic and energetic factors influencing assembly. As the number of particles increases, so does the complexity of the energy landscape, leading to longer assembly times. This emphasizes the potential for more intermediate metastable states in larger systems and the critical role of interaction energy in assembly efficiency. Next, we set to explore how the time to first assembly (T_{fas}) and stability (T_{stable}) depend on the patchy interaction potential (ϵ_{patch})

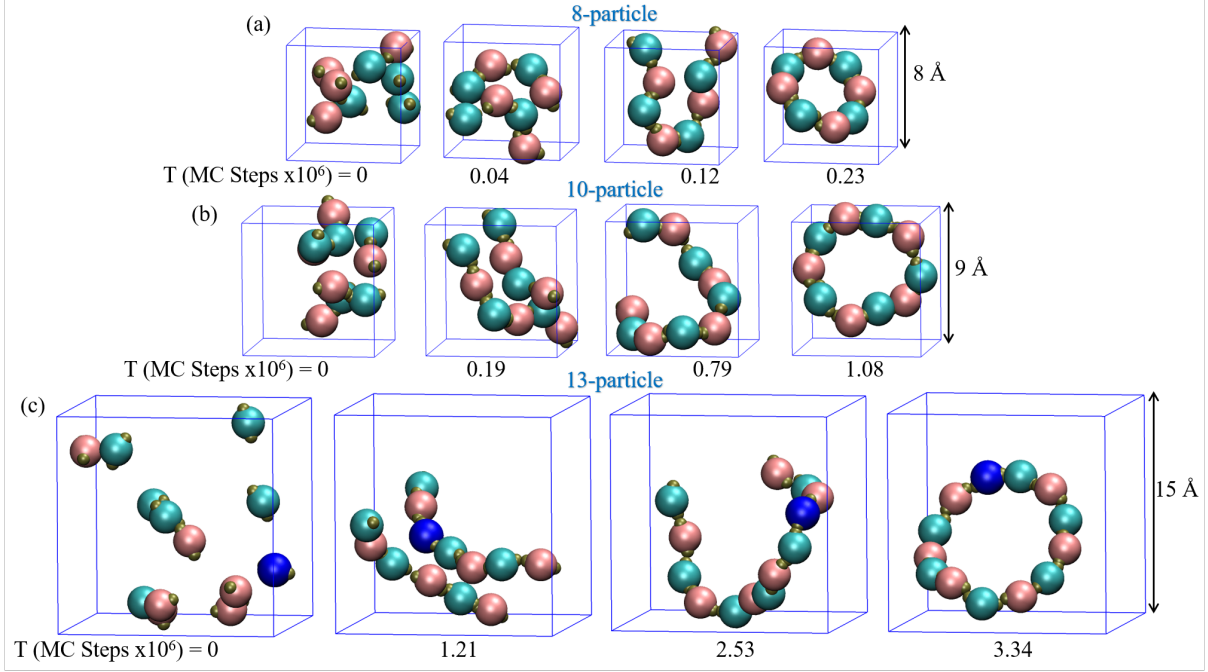


Figure 4: Equilibrium Monte Carlo simulation snapshots of (a) 8, (b) 10, and (c) 13 particles of type α (pink), β (cyan), and γ (blue), shown at various MC steps, starting from random initial conditions and ending at the assembly of the ring target structure. Sizes of the simulation boxes are shown.

across different system sizes.

3.1.1 Time to First Assembly in Equilibrium MC Simulations

In an attempt to calculate the time to reach the first assembly from random configurations to understand the inherent trade-off of equilibrium simulations, we carry out MC simulation over a wide range of ϵ_{patch} values, ranging from 0 to 50 kJ/mol. A temperature of 65 K corresponds to 0.54 kJ/mol ($k_B T$). Therefore, the range of ϵ_{patch} , between 0 to 50 kJ/mol, translates to a range of 0 to 93 ($\epsilon/k_B T$). For each value of ϵ_{patch} , the value of the time to first assembly, T_{fas} , is quantized in MC steps.

For the 8 particle (Fig.5(a)), 10 particle (Fig.5(b)), and 13 particle (Fig. 5(c)) systems, the median value of T_{fas} remains relatively constant at the simulation length (10×10^6 MC steps) at low interaction energies (ϵ_{patch}), suggesting that particles do not coalesce into a stable assembly within the allotted simulation time, with ϵ_{patch} ranges of 0 to 5 kJ/mol, 7

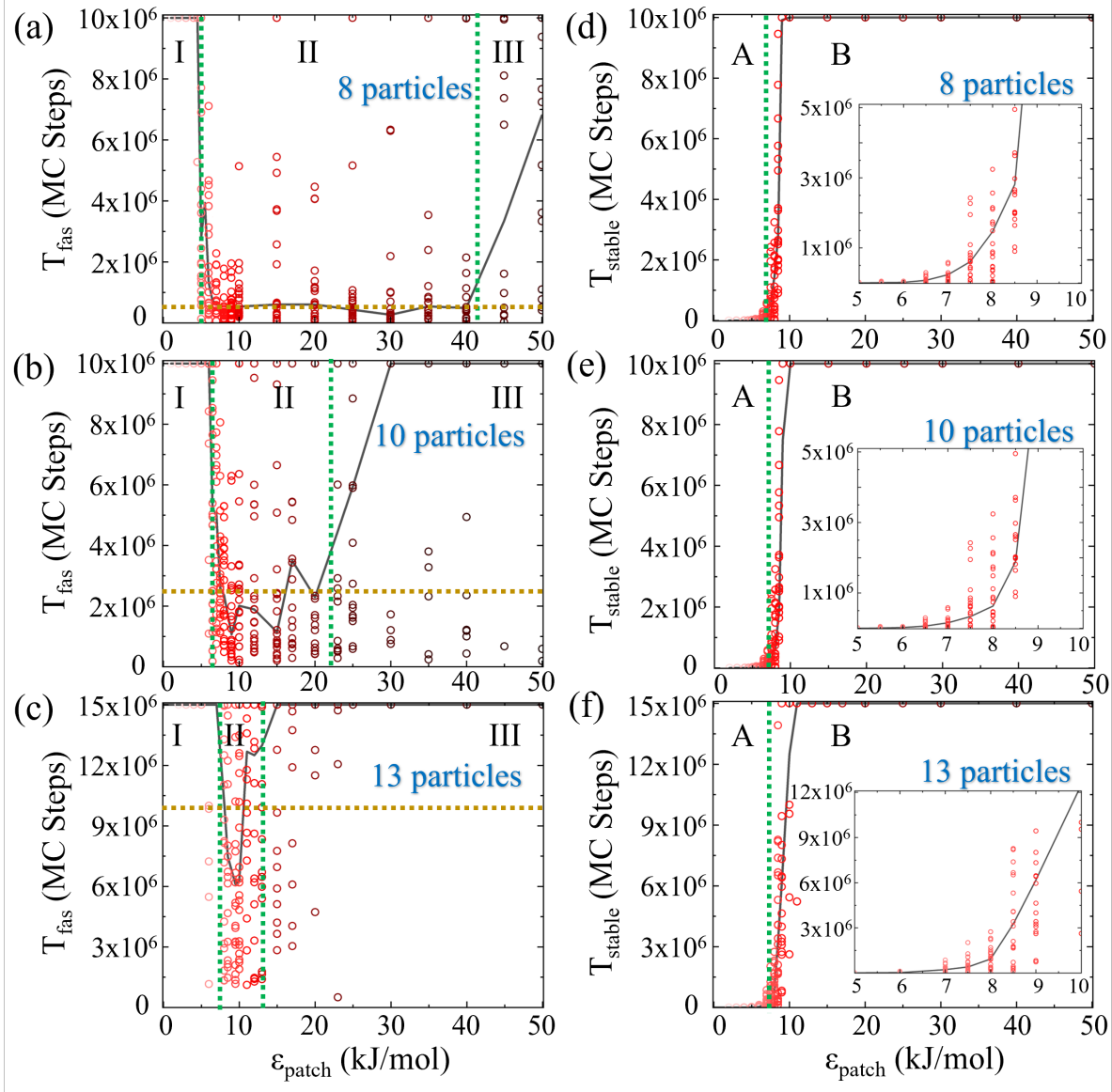


Figure 5: Equilibrium MC simulation results. Median T_{fas} values (black line) of 20 individual realizations (red circles), across different ϵ_{patch} values, for (a) 8 patchy particle system, (b) 10 patchy particle system, and (c) 13 patchy particle system. The ϵ_{patch} range is segmented into three regions (green dotted lines), with the average T_{fas} over the median values in the middle Region II depicted by a golden dotted line. Median T_{stable} values across different ϵ_{patch} values for (d) 8 patchy particle system, (e) 10 patchy particle system, and (f) 13 patchy particle system. The ϵ_{patch} range is categorized into two distinctive zones (green dotted lines). Insets: Zoom into the lower ϵ_{patch} range.

kJ/mol, and 8 kJ/mol, respectively. These low ϵ_{patch} ranges which hinder assembly formation are referred to as Region I (see corresponding Movies S1, S2, and S3, for 8, 10, and 13 patchy particles in the SI).

As ϵ_{patch} increases and falls within an intermediate range, a notable decrease is observed in T_{fas} . These ranges are 6 – 40 kJ/mol for the 8 particle system, 8 – 20 kJ/mol for the 10 particle system, and 8 – 12 kJ/mol for the 13-particle system. This decrease stabilizes to 0.7×10^6 , 2.1×10^6 , and 9.7×10^6 MC steps for the 8, 10, and 13 patchy particle systems, respectively, as indicated by the golden dotted lines in Figs. 5(a)-(c). These values are obtained by averaging over the median values of T_{fas} in the intermediate Region II. The observed narrowing of this optimal interaction energy range with increasing system complexity from 8 to 13 patchy particles can be attributed to the intricate potential energy landscapes in larger assemblies. As the number of particles grows, the likelihood of encountering metastable states increases, necessitating a more precise tuning of interaction energies to navigate toward the desired assembly. This intermediate region (designated as Region II) is identified as the optimal energy regime for assembly at equilibrium, where the majority of simulations successfully reach the target structure, albeit with an increase in T_{fas} .

At higher ϵ_{patch} values, T_{fas} begins to rise in all of the systems, suggesting that excessively strong interactions may be counterproductive, potentially trapping the system in kinetic traps. Significantly, for the 10 and 13 patchy particle systems, the median value of T_{fas} approaches the total number of MC steps, indicating more than half of the simulations fail to reach the target structure.

These trends across different interaction energy regimes highlight the delicate balance required for the self-assembly of patchy particles. Such insights are pivotal in advancing the fabrication of nanomaterials and the understanding of biological self-assembly processes where precise control over interaction energies is often beyond reach.

3.1.2 Target Stability in Equilibrium MC Simulations

The target stability is represented by the time the system remains in the target structure, T_{stable} . It is shown for systems comprising 8, 10, and 13 patchy particles in Figs. 5(d), 5(e), and 5(f), respectively. At low ϵ_{patch} values (Region A), all systems display relatively low

T_{stable} , indicating insufficient stability of the target structures. As ϵ_{patch} increases to values larger than $\sim 6 - 7$ kJ/mol (Region B), T_{stable} rises, indicating that the structures remain assembled throughout the entire simulation. For the 8-particle system, there is a sharp increase in T_{stable} beyond the critical threshold, while the 10 and 13-particle systems show a more gradual transition.

3.1.3 Analysis of Assembly Time and Stability in Equilibrium Self-Assembly

The dynamics of assembly and stability across the 8, 10, and 13 patchy particle systems under equilibrium conditions are influenced by interaction energy, ϵ_{patch} , as evident by the median values we have plotted. Plotting median values is necessary here due to the fact that in some regions of the parameter space, there were many realizations in which the target was not assembled (for T_{fas}) or disassembled (for T_{stable}), particularly in the case of low and high interaction energy values, which would bias the mean values. Therefore, showing the median ensures that the derived insights accurately reflect the typical system behavior. Low interaction energies prove insufficient for both assembly and stability across all systems, as indicated by the high values of T_{fas} (Region I) and low values of T_{stable} (Region A). At intermediate interaction energies, a clear decrease in T_{fas} (Region II) highlights the optimal range for self-assembly under equilibrium conditions. This range becomes narrower as system complexity increases from 8 to 10 and 13 patchy particles. In terms of target stability, beyond a ϵ_{patch} threshold, the assembled structure remains at the target state (Region B). Both T_{fas} and T_{stable} suggest a critical ϵ_{patch} range that balances the interaction energy necessary for assembly and subsequent stability, with larger systems requiring finer energy tuning to achieve and maintain assembled structures. At high interaction energies, an increase in T_{fas} (Region III) suggests that overly strong interactions may lead to kinetic traps and impede target structure formation. Concurrently, T_{stable} maintains its value equal to the simulation length for the higher values of ϵ_{patch} .

In the realm of equilibrium self-assembly, the behaviors within Regions I and A, charac-

terized by longer assembly times and low target stability, respectively, present a potential for external driving forces to play a critical role in accelerating the assembly while improving the stability of the targets. Such an intervention is particularly crucial in these regions, as it could overcome the limitations of equilibrium self-assembly, facilitating rapid assembly and longer stability. Furthermore, the range of interaction energy falling into the optimal region (Region II in Fig. 5) for any system depends on the system complexity, including its size, the nature of interactions, the parameters of patches, and the number density.

3.1.4 Time to First Assembly in Nonequilibrium MC Simulations

Nonequilibrium intervention in the form of an external drive has the potential to positively influence both the assembly speed and the target stability in Regions I and A, respectively. Here, we implement a driving force that favors the bond formation of nearest neighbor particles according to the target structure and disfavors bond breaking in this case.

In the 8-particle system (Fig. 6(a)) for ϵ_{patch} of 2 kJ/mol, T_{fas} remains at the maximum simulation length until ϵ_{drive} exceeds 3 kJ/mol, indicating that the system does not achieve the target structure without an adequate driving force. When ϵ_{drive} reaches 4 kJ/mol, T_{fas} is reduced significantly, suggesting that a specific threshold of an external drive is required to facilitate assembly. For ϵ_{patch} values of 3 and 4 kJ/mol, T_{fas} decreases to the equilibrium value of Region II (0.7×10^6 MC steps) once ϵ_{drive} exceeds 3 kJ/mol. A higher value of ϵ_{patch} (5-6 kJ/mol) leads to a relatively small T_{fas} even without an external drive, highlighting the importance of intrinsic interaction energy in assembly efficiency. In the later cases, a minimal ϵ_{drive} of 1 kJ/mol is adequate to reduce T_{fas} to its lowest observed plateau. To achieve similar reductions in T_{fas} for the 10-particle system, converging to the average T_{fas} value of the corresponding Region II (Fig. 5(b)), a higher ϵ_{drive} of 5 kJ/mol is required for ϵ_{patch} value of 2 kJ/mol. As ϵ_{patch} increases from 3 to 6 kJ/mol, lower ϵ_{drive} is required.

For the 13-particle system (Fig. 6(c)), T_{fas} remains at the simulation length value (15×10^6) without the intervention of external drive for all ϵ_{patch} values. An external drive of

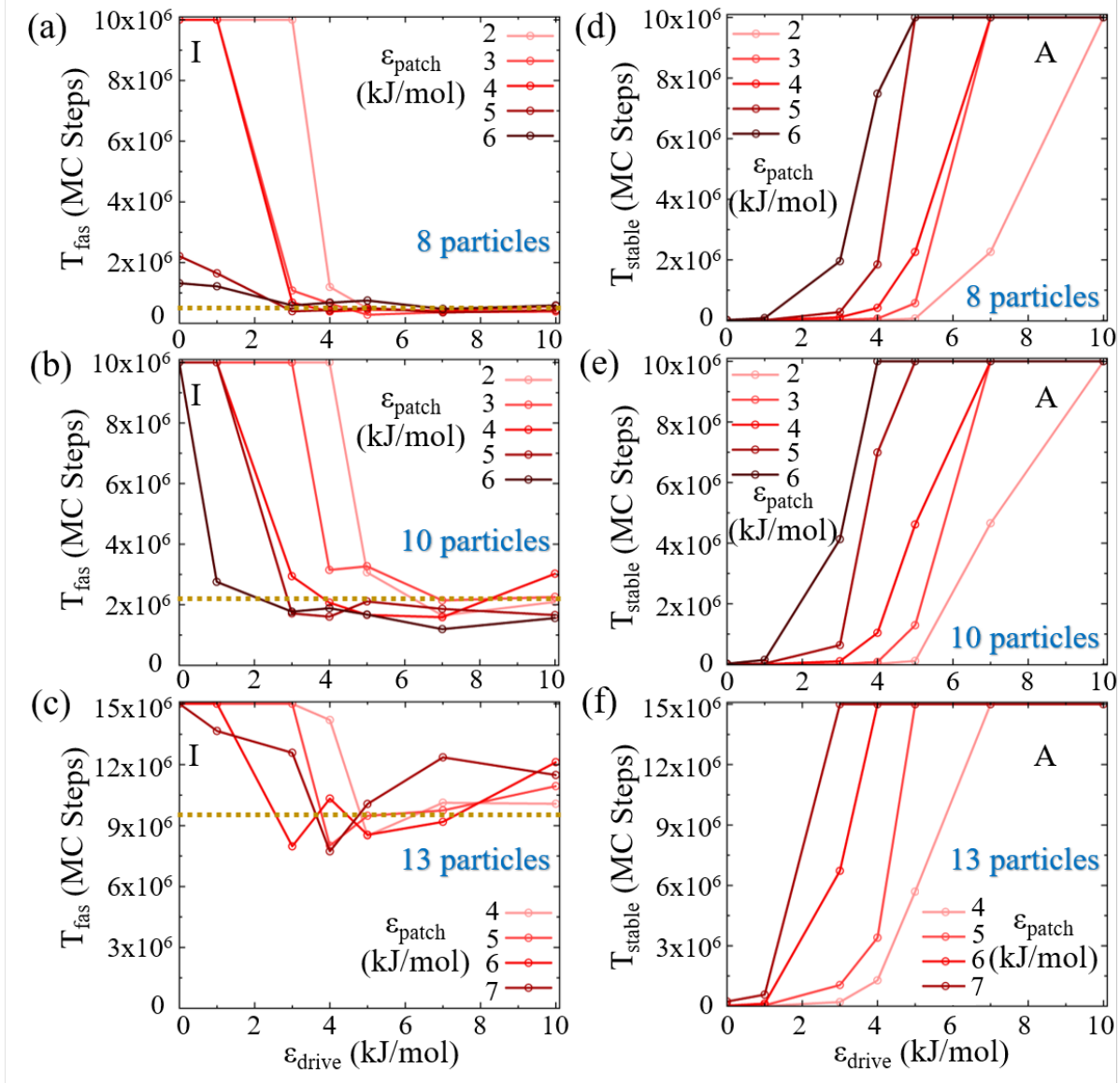


Figure 6: Nonequilibrium MC simulation results. Median T_{fas} values of 20 individual realizations for different patchy particle interaction energies, ϵ_{patch} , as a function of the drive value, ϵ_{drive} , for (a) 8 particle system, (b) 10 particle system, and (c) 13 particle system. The golden dotted line denotes the average value of T_{fas} in the intermediate Region II obtained from the corresponding results presented in Fig. 5(a)-(c). Median T_{stable} of 20 individual realizations for different patchy particle interaction energies, ϵ_{patch} , as a function of the drive value, ϵ_{drive} , for (d) 8 particle system, (e) 10 particle system, and (f) 13 particle system.

4 kJ/mol is needed at $\epsilon_{patch} = 4$ kJ/mol to reach the target, with higher ϵ_{drive} reducing T_{fas} to the equilibrium average value of Region II (Fig. 5(c)). As ϵ_{patch} increases from 5 to 7 kJ/mol, lower ϵ_{drive} values are needed.

Comparing the various system sizes, for ϵ_{patch} value fixed at 6 kJ/mol, a drive value ϵ_{drive} of 3 kJ/mol is required to reduce T_{fas} to its equilibrium value in the 13 particle system, where only 1 kJ/mol is required to achieve the same result in a 10 particle system, and the 8 particle system archives the equilibrium value without any external drive.

These simulations show that external drives can effectively reduce the assembly times up to a point where an increase in the driving force does not result in additional acceleration. This suggests that while external driving forces can enhance assembly speed, there exists a limit to their efficacy beyond which the system behaves similarly to the equilibrium systems observed in the corresponding Region II. For a visualization of the nonequilibrium self-assembly process, see Movies S4, S5, and S6, for 8, 10, and 13 patchy particles, respectively, in the SI.

3.1.5 Target Stability in Nonequilibrium MC Simulations

The external drive also increases the target stability, manifested in higher T_{stable} for increasing drive values for several ϵ_{patch} values within the corresponding Region A for all systems tested, of 8 (Fig. 6(d)), 10 (Fig. 6(e)), and 13 (Fig. 6(f)) patchy particles, aligning with previous findings.^{96,98,99}

In the 8-particle system (Fig. 6(d)), at $\epsilon_{patch} = 2$ kJ/mol, T_{stable} gradually increases with ϵ_{drive} , aligning with the simulation length (10×10^6 MC steps) beyond 5 kJ/mol. As ϵ_{patch} increases from 3 to 6 kJ/mol, lower ϵ_{drive} values suffice to enhance T_{stable} , indicating higher internal interaction energies improve stability. For the 10-particle system (Fig.6(e)), T_{stable} at $\epsilon_{patch} = 2$ kJ/mol increases only beyond $\epsilon_{drive} = 6$ kJ/mol, with higher ϵ_{patch} reducing the needed ϵ_{drive} . In the 13-particle system (Fig.6(f)), at $\epsilon_{patch} = 4$ kJ/mol, $\epsilon_{drive} = 3$ kJ/mol significantly increases stability. For higher ϵ_{patch} values, modest increases in ϵ_{drive} ensure maximal stability.

3.1.6 Analysis of Nonequilibrium Self-Assembly Mechanism

We now turn to explore the assembly dynamics of patchy particles under external forces by focusing on an order parameter (R) and the total entropy production (S)¹²² as a function of MC steps. R is defined as the ratio of the number of formed bonds at any given MC step to the total number of bonds in the target structure, therefore quantitatively characterizes the path to assembly. The detailed description of the computation of S in our MC simulation is provided in Section S1 of the Supporting Information (SI).

The evolution of R for a 10 patchy particle system with patch interaction value of $\epsilon_{patch} = 3$ kJ/mol, under equilibrium, $\epsilon_{drive} = 0$, and nonequilibrium conditions, $\epsilon_{drive} = 7$ kJ/mol, is depicted in Fig. 7(a) and Fig. 7(b), respectively. In the absence of an external drive, R displays stochastic behavior, oscillating between 0 and 0.6, manifesting the inability of the system to assemble the target. With the external drive, a stark transition in the behavior of the order parameter is observed, with R ascending from a disordered state directly toward the fully assembled target structure, corresponding to $R = 1$ at 3.7×10^6 MC steps. The quantized changes in R represent the discrete steps of the subsequent formation of 10 bonds, ultimately yielding the 10 particle ring structure.

Similarly, the total entropy production, S , exhibits fluctuations at equilibrium (Fig. 7(c)), indicating vanishing entropy production rate, as expected.¹²² Under nonequilibrium conditions, the value of S rapidly increases (Fig. 7(d)), reflecting the dissipation of energy accompanying the utilization of the external drive.

The contrast in the behavior of R and S with and without an external driving force emphasizes the significant role of external driving forces in directing the thermodynamic path of patchy particle systems. The external drive enhances the order within the system at the cost of the production of entropy.¹²³ Similar observations for trajectories of 8 and 13 patchy particles in equilibrium and nonequilibrium MC simulations can be found in Figs. S1 and S2 in Section S2 of the SI.

The effect of the external drive is quantified by $T_{enhance}$, defined as the ratio of the median

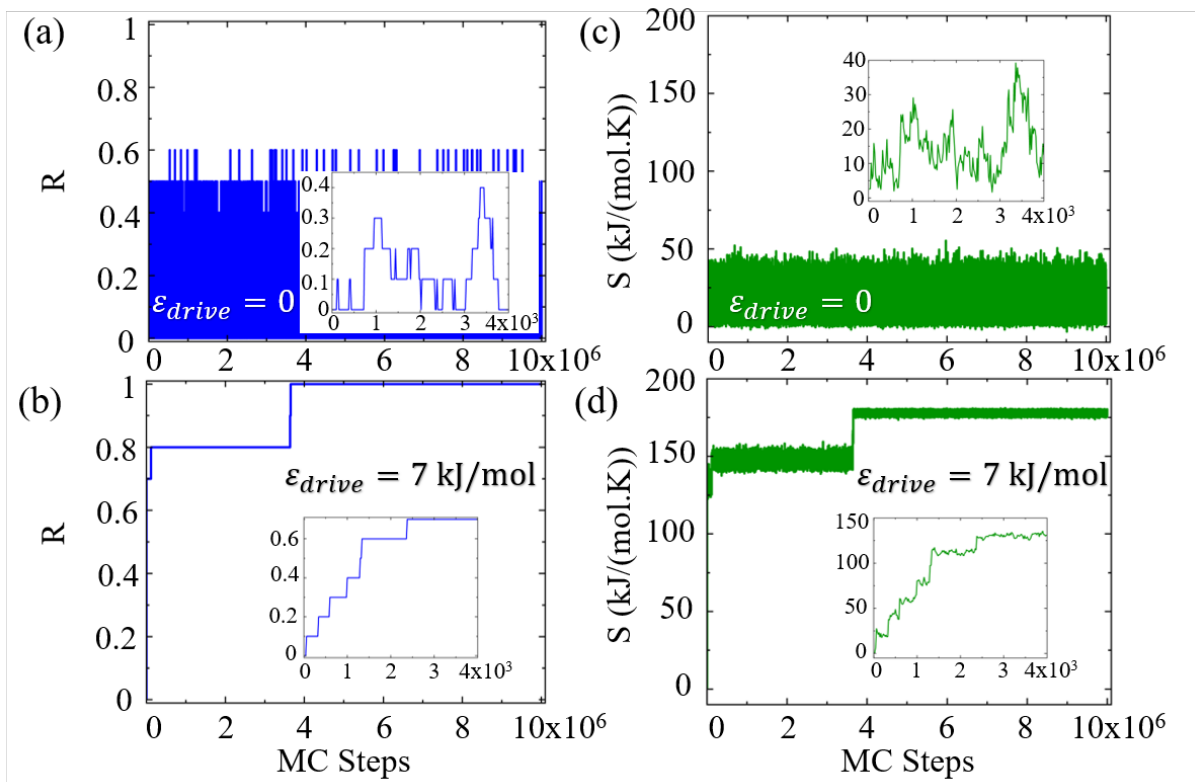


Figure 7: Order parameter (R) as a function of MC steps (a) in equilibrium and (b) under nonequilibrium conditions with an external drive $\epsilon_{drive} = 7$ kJ/mol. The total entropy production (S) as a function of MC steps (c) in equilibrium and (d) under nonequilibrium conditions with an external drive $\epsilon_{drive} = 7$ kJ/mol. Results are presented for a single MC realization of 10 particle system with $\epsilon_{patch} = 3$ kJ/mol. The inset plots show Zoom in into the early simulation steps.

time to the first assembly with the external drive (ϵ_{drive}) to the median time without the drive, across a set of 20 distinct simulations for a given value of ϵ_{patch} . This metric provides a measure of the efficiency improvement in assembly time attributable to the external drive. For example, this metric for 8 particles is obtained from the values plotted in Fig. 6(a) for a given system. For the 8 particle system (Fig. 8(a)), $T_{enhance}$ shows a significant increase with increasing ϵ_{drive} , showing approximately 35 fold improvement in the assembly time compared to the equilibrium assembly for $\epsilon_{patch} = 3$ kJ/mol, for example. In the 10 particle system (Fig. 8(b)), an increase in $T_{enhance}$ with rising ϵ_{drive} is observed, with more modest improvement in assembly time. The enhancement reaches a plateau at about 6 to 8 fold

improvement, occurring at an ϵ_{drive} near 6 kJ/mol. The variation of $T_{enhance}$ of 13 particle system is displayed in Fig.8(c), achieving a moderate improvement of up to 2-fold in the assembly time compared to the equilibrium scenario. Compared to the increase of $T_{enhance}$ for 8 and 10 particle systems with the increase in drive, the increment for the 13-particle system does not show similar improvement with increasing the drive value. This reflects the more complex assembly pathway involving 13 patchy particles and multiple interaction types: $\alpha - \beta$, $\alpha - \gamma$, and $\beta - \gamma$, compared to only $\alpha - \beta$ interaction between the other two smaller systems. The enhancement factors $T_{enhance}$ are presented along the ratio of T_{fas} from Region I to T_{fas} in Region II in equilibrium simulations (Fig. 8, dotted lines), further indicating that the drive helps the system achieve its target within the time frame that matched the one of the optimal region (Region II).

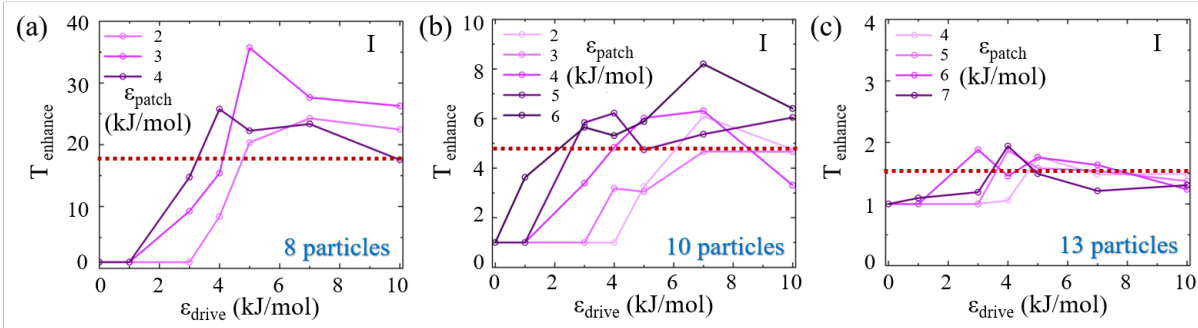


Figure 8: $T_{enhance}$ as a function of ϵ_{drive} for various ϵ_{patch} values from Region I for systems of (a) 8 particle, (b) 10 particle, and (c) 13 particle systems. The brown dotted line represents the ratio of T_{fas} between Regions I and II, obtained from the corresponding results in Fig. 5(a)-(c).

In order to test the effects of our chosen patch size and particle density parameters,^{76,124} we explore the time to first assembly and target stability for various values of the length of the patch, $\delta/2$ (Section S3 in the SI) and different lengths of the simulation cell (Section S4 in the SI). Importantly, the trend of T_{fas} and T_{stable} under both equilibrium and nonequilibrium conditions remains similar, and our conclusions hold for the different cases.

3.2 Molecular Dynamics Simulation Results

Transitioning into the MD simulations, we expand upon the findings from the MC simulations to further explore the dynamic aspects of dissipative self-assembly of the patchy particle system under both equilibrium and nonequilibrium conditions. MD simulations, with their capacity to capture real-time dynamics, are instrumental in providing a more thorough understanding of the mechanisms at play. This approach complements the MC results by offering insights into the temporal evolution of particle assemblies, thereby enriching our analysis with a perspective that closely mirrors physical realities.

Moreover, the implementation of nonequilibrium MD simulations is a deliberate effort to bridge the computational findings with potential experimental validations. By examining the system’s response to external drives and the resultant dynamic behaviors, this segment aims to not only complement the MC-derived thermodynamic landscapes but also to lay a foundational basis for future experimental investigations.

3.2.1 Equilibrium MD Simulations

We first set to explore the time to reach the target structure starting from random initial conditions within the simulation box for systems of 8 and 10 patchy particles with a single internal state, α . The time to first assembly, T_{fas} , is calculated over a broad range of interaction energies between patches, ϵ_{patch} , ranging from 0 to 100 kJ/mol. Similar to the approach taken in our equilibrium MC simulations (refer to Section 3.1.1), the behavior of T_{fas} as a function of ϵ_{patch} can be categorized into three distinct regions. At low ϵ_{patch} values, the system is unable to achieve the target structure within the allotted simulation time of 12000 ps due to the weak interaction (Region I), whereas for larger ϵ_{patch} values, T_{fas} decreases, manifesting an optimal range for assembly (Region II). Beyond a particular ϵ_{patch} value, T_{fas} begins to rise, signifying the onset of kinetic trapping that inhibits the particle reorientation towards the target structure (Region III).

For the 8 particle system (Fig. 9(a)), no assembly occurs for ϵ_{patch} values between 0 to

6 kJ/mol (Region I). Beyond 6 kJ/mol, T_{fas} decreases and stabilizes at 5115 ps (Region II), until approximately 40 kJ/mol (Region III), where T_{fas} increases up to the simulation duration (Movie S7 in the SI). Similar results with 8 patchy particles with hard-sphere interaction were observed in our concurrent study,¹²³ where T_{fas} transitioned from Region II to III above 40 kJ/mol value of ϵ_{patch} .

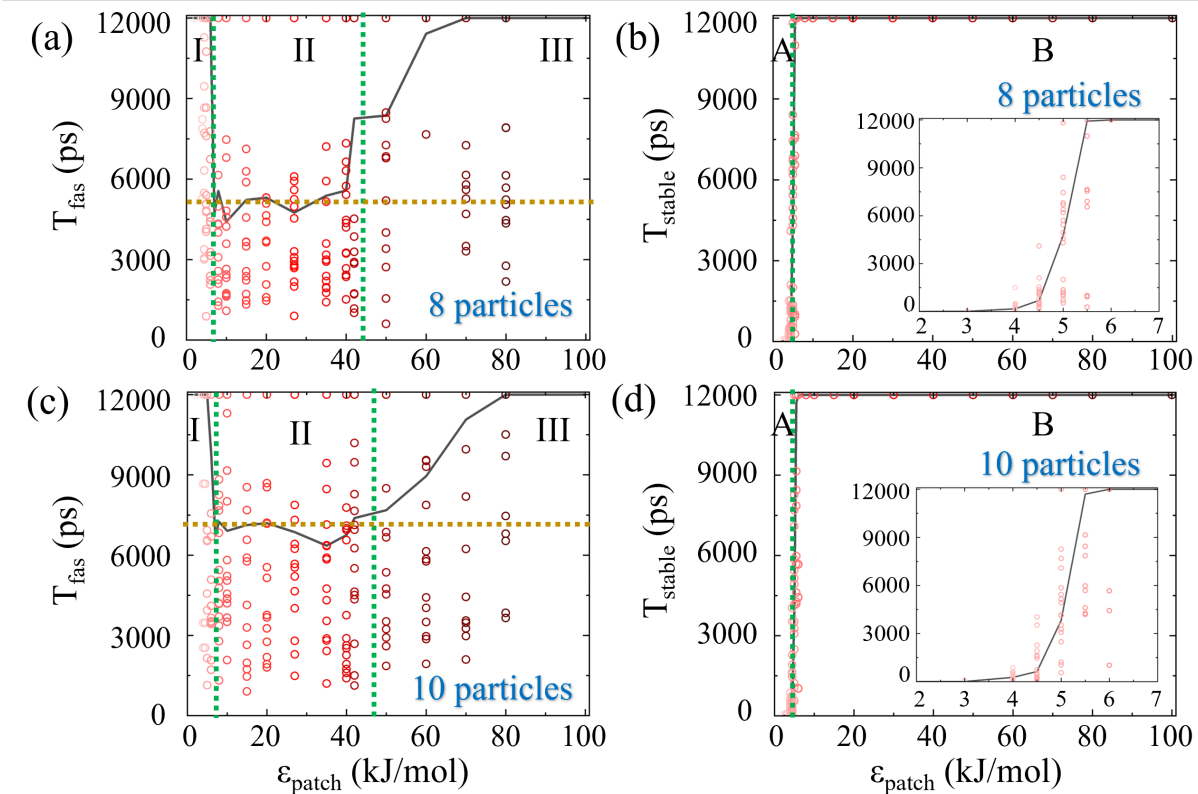


Figure 9: Equilibrium MD simulation results. Median T_{fas} values (black line) of 20 individual realizations (red circles), across different ϵ_{patch} values, for (a) 8 patchy particle system and (b) 10 patchy particle system. The ϵ_{patch} range is segmented into three regions (green dotted lines), with the average T_{fas} over the median values in the middle Region II depicted by a golden dotted line. Median T_{stable} values across different ϵ_{patch} values for (c) 8 patchy particle system, and (d) 10 patchy particle system. The ϵ_{patch} range is categorized into two distinctive zones (green dotted lines). Insets: Zoom into the lower ϵ_{patch} range.

In addition to the time to reach the assembled state, we set to study the stability of the resulting target structure by the time the system remains at the target state, T_{stable} , in a set of simulations initiated at the target across the same ϵ_{patch} range. As for the MC simulations (Section 3.1.2), the behaviors of T_{stable} clearly segment the ϵ_{patch} values into the

regions, where for low ϵ_{patch} values the target quickly disassembles (Region A), whereas for higher values, the target remains stable (Region B).

In the case of the 8 particle system (Fig. 9(b)), for ϵ_{patch} values up to 4 kJ/mol, T_{stable} is minimal (a few ps), indicating low system stability. However, as ϵ_{patch} increases, the median T_{stable} rises and reaches the full duration of the simulation (12000 ps) by $\epsilon_{patch} = 6$ kJ/mol. These observations lead to the classification of Region A to include ϵ_{patch} values between 0 - 6 kJ/mol, and Region B between ϵ_{patch} values of 7 - 100 kJ/mol.

The same methodology is applied to a system of 10 patchy particles with a single internal state, α . The trend of T_{fas} as a function of ϵ_{patch} mirrors the behavior of the 8 patchy particle system (Fig. 9(c)), and the ϵ_{patch} range was similarly segmented into Region I (0 - 6 kJ/mol), Region II (7 - 50 kJ/mol), and Region III (50 - 100 kJ/mol). The average of median T_{fas} in Region II is 7024 ps, shown as a golden dotted line, which is slightly higher than that of the 8 patchy particle system owing to its lower complexity. As for the stability of the resulting target quantified by T_{stable} (Fig. 9(d)), we observe low target retention of only a few ps for low ϵ_{patch} values (Region A). When ϵ_{patch} exceeds 4 kJ/mol, the median T_{stable} rises and reaches the full simulation duration (12000 ps) at 6 kJ/mol (Region B), (See Movie S8 in the SI).

As argued in Section 3.1.3, Regions I and A are characterized by prolonged assembly times and reduced structural stability, respectively, thereby presenting an opportunity for an external bias to overcome these equilibrium limitations and to enable quicker self-assembly and improved target stability.

3.2.2 Nonequilibrium MD Simulation Results

In nonequilibrium MD simulations, we explore the influence of an external drive in the form of an external square wave potential with varying amplitude, $U_{square}(t)$, added to the patchy interaction potential, $U_{patch}(r)$, on the assembly dynamics for systems of 8 and 10 patchy particles. The amplitudes of $U_{square}(t)$ ranges from 0 to 60 kJ/mol, for patchy interaction

ϵ_{patch} values of 4.5, 5, and 6 kJ/mol from Regions I and A. For each scenario, we determine the time to the first assembly, T_{fas} , and the target stability, T_{stable} .

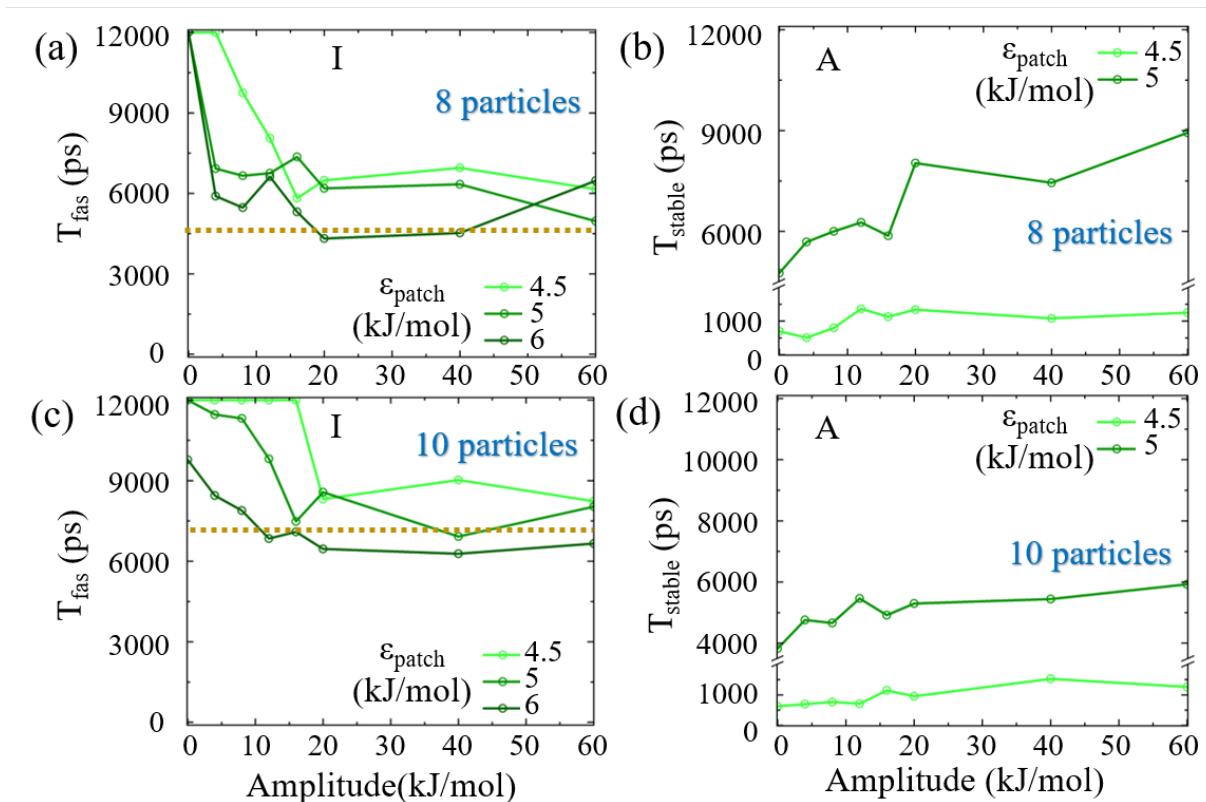


Figure 10: Nonequilibrium MD simulation results. Median T_{fas} values of 20 individual realizations for different patchy particle interaction energies, ϵ_{patch} , as a function of the amplitude of the square wave potential for (a) 8 particle system, and (c) 10 particle system. The golden dotted line denotes the average value of T_{fas} in the intermediate Region II obtained from the corresponding results presented in Fig. 9(a) and (b). Median T_{stable} of 20 individual realizations for different patchy particle interaction energies, ϵ_{patch} , as a function of the amplitude of the square wave potential for (b) 8 particle system, and (d) 10 particle system.

For 8 particle system with $\epsilon_{patch} = 4.5$ kJ/mol, T_{fas} significantly reduces for external drive amplitudes above 4 kJ/mol, where for amplitude value of 20 kJ/mol and beyond, T_{fas} drops to around 6000 ps (Fig. 10(a)). For ϵ_{patch} values of 5 and 6 kJ/mol, T_{fas} immediately shows a significant decrease to around 6000 ps (Movie S9 in the SI). This value is similar to the average T_{fas} of approximately 5100 ps obtained in Region II of 8 patchy particle equilibrium MD simulations (Fig. 9(a), golden dotted line).

In terms of stability of 8 particle system, for ϵ_{patch} of 4.5 kJ/mol, T_{stable} is 700 ps at zero amplitude (Fig. 10(b)), and increases to 1200 ps as the amplitude of the external drive increases to 12 kJ/mol and further. At 5 kJ/mol, T_{stable} rises from 4000 ps to 9000 ps with an increasing amplitude of up to 60 kJ/mol. These results indicate that the introduction of an external square wave potential can substantially enhance stability for the 8 patchy particle system.

To further complement our study, we conduct MD simulations for a 10 patchy particle system, considering the influence of an external square wave potential. At $\epsilon_{patch} = 4.5$ kJ/mol, T_{fas} remains largely unchanged until the potential amplitude exceeds 20 kJ/mol, then fluctuates around 7500 ps (Fig. 10(c), Movie S10 in the SI). At $\epsilon_{patch} = 5$ kJ/mol, T_{fas} decreases from 12000 ps to 9000 ps at 16 kJ/mol amplitude, and further to 7000 ps at 60 kJ/mol. For $\epsilon_{patch} = 6$ kJ/mol, T_{fas} decreases from 10000 ps to 6000 ps as the amplitude increases to 12 kJ/mol, suggesting a greater sensitivity of the assembly time to the applied potential in comparison to the lower ϵ_{patch} values. These findings align with the average T_{fas} values observed in Region II of the equilibrium MD simulations for the 10 patchy particle system (Fig. 9 (c), golden dotted line).

The stability of the 10 patchy particle system under nonequilibrium conditions is analyzed by varying the amplitude of the external drive while initiating the system at target under ϵ_{patch} values of 4.5 and 5 kJ/mol (Fig. 10(d)). The value of T_{stable} increases from 520 ps to 1100 ps as the amplitude is increased from 0 to 16 kJ/mol, where further increment in amplitude does not result in an additional increase in T_{stable} . For ϵ_{patch} value of 5 kJ/mol, the stability time T_{stable} rises from 4000 ps to 6000 ps with a modest amplitude increment to 10 kJ/mol. Similarly, subsequent increases in the amplitude do not enhance T_{stable} significantly.

Comparing the 8 and 10 patchy particle systems in nonequilibrium MD conditions, we notice distinct responses to the external drive. Both systems experience reduced assembly times (T_{fas}) as the amplitude of the square wave potential increases. The 10 patchy particle

system, however, shows a higher sensitivity to the amplitude changes, necessitating finer tuning in driving forces for comparable reductions in T_{fas} . This size-dependent response highlights how system complexity affects the dynamics of self-assembly, similar to our observation in the nonequilibrium MC simulations. Further, stability analysis (T_{stable}) reveals that while the stability improves for both systems with higher drive amplitudes, the enhancement is less pronounced in the 10 patchy particle system. In contrast to the nonequilibrium MC simulations, where the stability (T_{stable}) is maintained throughout the entire simulation, the nonequilibrium MD simulations reveal further opportunities for improvement. This suggests that optimizing the effectiveness of the square wave potential as an external driving force can potentially further increase target stability.

The acceleration of the assembly and the improved target stability we find in our MD simulations are also manifested in the analysis of the order parameter, R , defined in a similar way as for the MC simulations, as the ratio between the number of formed bonds to the total number of bonds in the target structure. We calculate the value of R averaged over the entire simulation duration and observe a moderate increase when the time-dependent square wave potential is introduced to the system, for systems of 8 and 10 particles (Section S5 in the SI).

In our investigation of assembly kinetics and stability under nonequilibrium conditions using MD simulations, we meticulously analyze the behavior of bond formation and dissociation events across both high and low energy phases induced by the square wave potential, $U_{square}(t)$. From this analysis, we observe that the bond durability in our patchy particle system is enhanced with the increase of square wave amplitudes, which in turn boosts the stability of the target structure and aids in its assembly (Section S6 in the SI).

3.2.3 Potential Energy and Force Comparison of 2 Particle System

In order to better understand the dynamics of bond formation, we conduct a set of MD simulations of a system comprising only 2 particles randomly initiated up to the first bond

formation event in equilibrium and nonequilibrium conditions. During the simulation realizations, we track the total potential energy of the system and the force between the particles. For this study, the simulation cell dimensions are set to $2 \times 6 \times 6 \text{ \AA}^3$, with patch parameters identical to those in a 10 particle system. Apart from the simulation cell size, all simulation parameters are consistent with those used in simulations of the 8 and 10 patchy particle systems. Importantly, the outcomes do not strictly depend neither on the dimensions of the simulation cell nor on the patch parameters ($\delta/2$ and θ^{\max}).

Under equilibrium conditions for patchy interaction energies ϵ_{patch} of 5 kJ/mol (Fig. 11(a)) and 6 kJ/mol (Fig. 11(b)), the potential energy initially fluctuates around 0, and the corresponding force between the particles, reflecting the gradient of the potential energy, also remains close to 0. On the other hand, the bond formation event, which occurs at 294 ps and 1132 ps for ϵ_{patch} of 5 kJ/mol and 6 kJ/mol, respectively, is manifested in a noticeable decrease of the potential and a concurrent force spike.

In stark contrast, nonequilibrium conditions exhibit a completely different profile of the total potential energy and the force for both patchy interaction energies of 5 kJ/mol (Fig. 11(c)) and 6 kJ/mol (Fig. 11(d)). Here, the potential energy is characterized by significantly larger fluctuations owing to the varying high and low energy phases of square wave potential, resulting in larger forces acting between the two particles compared to the corresponding equilibrium values. The particles are, therefore, subject to frequent and substantial energy changes, driving them to reorient and adjust their positions as they seek stable configurations. The difference in the force magnitudes between equilibrium and nonequilibrium underscores the mechanism of the increased bond-formation events observed in Fig. S7. These larger forces in the nonequilibrium state catalyze the movement of particles toward each other, expediting the bonding process.

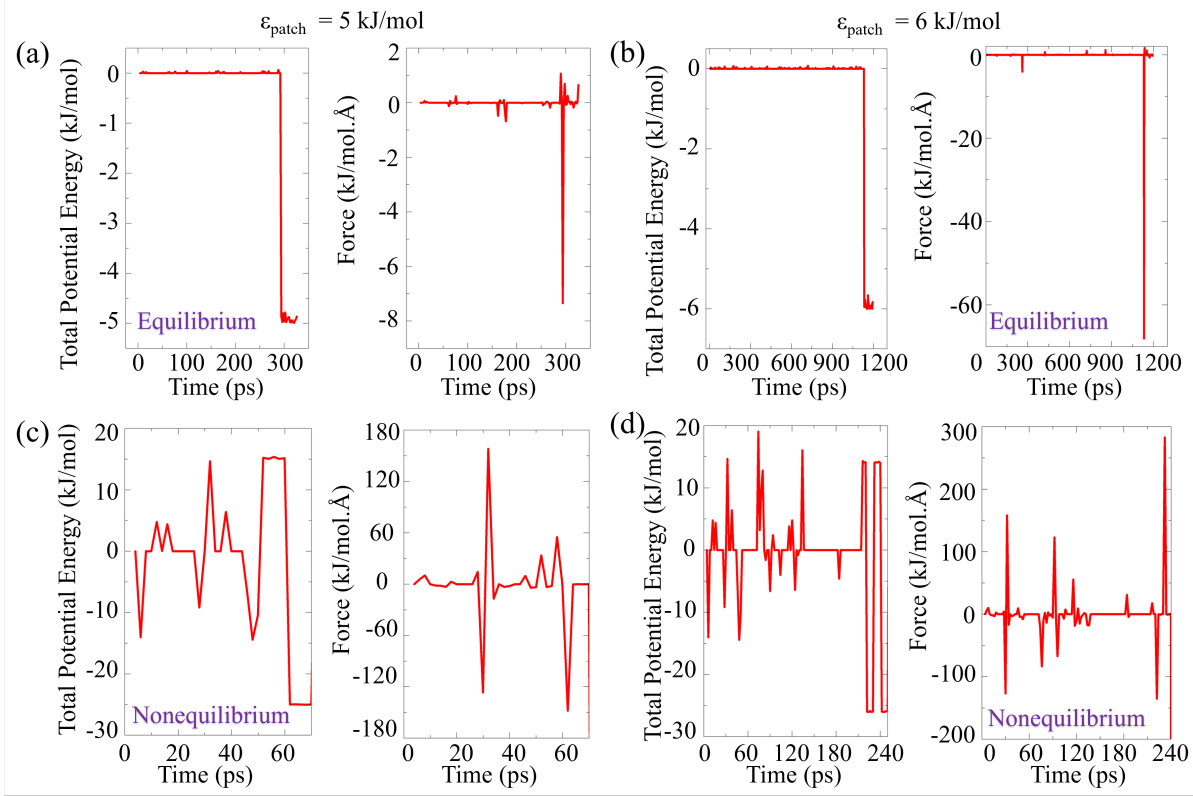


Figure 11: MD simulation of a 2 particle system up to the first bond formation event. Total potential energy and force as a function of time for equilibrium conditions with ϵ_{patch} value of (a) 5 kJ/mol and (b) 6 kJ/mol, and nonequilibrium conditions with square wave potential amplitude of 20 kJ/mol for ϵ_{patch} value of (c) 5 kJ/mol and (d) 6 kJ/mol, shown for individual realizations.

3.3 Effect of External Drive on Self-Assembly of Large Systems

In order to demonstrate the efficacy of our proposed design principle of applying an external nonequilibrium drive for a large-scale system, we ran both equilibrium and nonequilibrium simulations of 100 patchy particles (Section S7 in the SI). The particles were modeled with PHS interaction between patches and PBC of the simulation cell to examine how interaction energies ϵ_{patch} and ϵ_{drive} influence the structure formation. The patches in these simulations were positioned with an interior angle of 135 degrees for 8-ring formations and 90 degrees for 4-ring formations to explore the ring formation in the resultant assembly structure subjected to different patch orientations, using other parameters similar to those in smaller-scale systems of 8 patchy particles.

The equilibrium (Fig. S8(a)) and nonequilibrium (Fig. S8(b)) results for the larger system of 100 particles are consistent with the observations of our smaller systems of 8, 10, and 13 patchy particles, showing faster bond formation in the presence of the drive compared to the corresponding equilibrium results with similar interaction strength between the patches. Similar observations have been showcased in Figs. S9(a) and S9(b) for large systems with 4-ring specifications. The overall results are consistent with the small-scale system, demonstrating that using an external drive can facilitate a faster assembly process in the region of weak ϵ_{patch} . Thus, our approach of nonequilibrium drive is independent of the overall system size, effectively negating any finite-size effects and emphasizing the robustness of our assembly protocol.

It is important to note that the formation of rings strictly depends upon the system parameters, particularly on the patch orientation and the number density of the system. While the system with a patch orientation corresponding to an 8-ring structure produces open rings or chains (Movie S11), the systems with a patch orientation of a 4-ring produce rings (Fig. S9(c) and Movie S12). Moreover, adding an external drive to the system in the latter case increases the number of rings formed for weak patchy interactions where no structure formation occurs without the drive (Fig. S9(d)), similar to our previous observations.

We also conducted an equilibrium MD simulation of a 4-ring specific system comprising 100 particles, utilizing PHS interactions and PBC for the simulation cell (Fig. S10). This simulation corroborated the structural formations observed in our MC simulation results, as shown in Fig. S8(a), thereby validating the consistency and reliability of our findings across different simulation methodologies.

Since our external drive depends only on the interaction between patches that are nearest neighbors in the predefined target structure, it can only accelerate the structure formation observed in equilibrium simulations, as the nature of the formed structure strictly depends on internal system parameters. Additionally, while increasing the specificity of patchy interactions can impact the optimal interactions for assembly rate and stability timescales, it

has no effect on the mechanism of the external drive employed in our design. Therefore, a careful balance of specificity and robustness is necessary for optimal self-assembly processes.

4 Conclusions

In our study, we embarked on an exploration to discern the limitations posed by equilibrium conditions in self-assembly processes, and how external drives could alleviate these challenges. Motivated by both biological self-assembly processes (particularly of actin filament and microtubules) and experimental observations, we introduce an external stimulus to a model system of self-assembling patchy particles, to study the resulting dissipative self-assembly. To generalize the findings from this study in the future to specific biological systems, patchy particles have been employed here as it has already been shown to closely mimic the dynamic behavior of actin filament and microtubule structure.^{125,126} Through a synergistic approach combining both MC simulations and MD simulations, under equilibrium and nonequilibrium conditions, our objective was to elucidate the impact of the nonequilibrium external drive on the dynamics of the system. This involved a detailed examination of trajectory realization and an analysis of the fundamental mechanisms driving the observed behaviors.

Our findings reveal that the equilibrium MC simulations of patchy particles with 8, 10, and 13 particles exhibit low assembly rates and low structural stability for weak patchy particle interactions. The external drive greatly improved the time to assembly and increased the structural stability of the target for the weak interactions regime, reaching the optimal values obtained at equilibrium for a narrow range of the patch interaction energies. This extends the ability of the system to assemble the target for a wider range of conditions compared to the equilibrium scenario, owing to the nonequilibrium external drive.^{96,98,99} The order parameter (R) and total entropy production (S) along with the realizations demonstrated how the external drive guided the system from a disordered initial state to the order configuration of the target structure.

Our detailed investigation revealed that the complexity of the system influences the self-assembly process in both equilibrium and nonequilibrium conditions. As the complexity increased to a larger number of particles in the system, the effect of the drive was smaller in terms of the final assembly rates and structural stability. We hypothesize that as complexity increases, the multitude of potential interaction pathways and configurations may lead to kinetic trapping or interference, thereby diminishing the influence of the external stimuli. Consequently, this emphasizes a substantial opportunity for improving the design principles of incorporating external stimuli, ensuring they are dynamically responsive to the increasing complexity of the system. Furthermore, the impact of patch length and number density on the self-assembly dynamics of patchy particles had no significant effects on the assembly time and structural stability of the target.

To further extend our conclusions, we employed MD simulations of self-assembling patchy particles with a periodic square wave potential as an external drive, inspired by the experimental applications of varying external fields.^{84,85} This approach demonstrated similar trends in the acceleration of the assembly and the increase in target stability, mirroring our MC simulation results. While the effect of the drive brought the system to the optimal performance level at equilibrium, its importance was in the ability to allow for rapid assembly and increased stability in a wider parameter range, i.e., lower values of the patch interaction energy, not possible in equilibrium without the external driving. Furthermore, the dynamic properties such as translational and rotational diffusivity are influenced by the mass of the particles and patches, but the relative behavior between equilibrium and nonequilibrium conditions remains qualitatively consistent regardless of the mass ratio. Additionally, an analysis of particle forces and bond dynamics in the presence of the nonequilibrium drive indicated that large momentary forces were responsible for bond formation and stability. Future efforts will include a comprehensive sensitivity analysis of additional system parameters, including the number of particle states, angular dependencies, and varying boundary conditions, to fully understand their impact on self-assembly dynamics.

Our study contributes to the understanding of how external drives can be strategically employed to circumvent the equilibrium limitations in self-assembly processes. By employing the LJ potential with different internal states and reflective boundary conditions in MC simulations and the PHS potential with a single internal state and PBC in MD simulations for smaller systems (8, 10, and 13 patchy particles), we demonstrate the versatility and effectiveness of our design protocol across varying conditions. This approach highlights the robustness of our protocol in achieving faster and more stable assembly, regardless of the simulation method employed. Additionally, to ensure that the choice of boundary conditions does not significantly affect our results, we conducted simulations of 100 particles using PBC in both MC and MD simulations. The outcomes showed similar results, indicating that the qualitative behavior of assembly remains consistent across different boundary conditions. The use of a square wave as a model for external stimuli opens avenues for experimental implementation, offering insights into experimental observations and applications of patchy particles, which can be implemented across various systems, such as colloids and block copolymers.^{22,65,71}

Looking forward, a deeper understanding of dissipative self-assembly mechanisms will push the development of novel synthetic nanostructures for numerous applications. Furthermore, the effects of various external forces on the self-assembly process are worth exploring. For instance, alternating electric or magnetic fields could influence particle orientations and interactions, potentially leading to assembly structures overcoming equilibrium limitations. Stochastic perturbation is another choice of external force that might introduce randomness that can hinder or enhance the assembly process. This exploration will also need to consider how these forces are influenced by key parameters such as system size, patch-patch interactions, and binding affinity between different patchy particles to comprehensively understand their impact on self-assembly. By gaining all these insights, we will extend our approach from simplified models of patchy particles to more complex representations of biological proteins and explore their self-assembly under external influences.

Acknowledgement

G.B. acknowledges the Zuckerman STEM Leadership Program and the Tel Aviv University Center for AI and Data Science (TAD). This work was supported by the ERC NanoNonEq 101039127, the Air Force Office of Scientific Research (AFOSR) under Award No. FA9550-20-1-0426, and by the Army Research Office (ARO) under Grant No. W911NF-21-1-0101. The views and conclusions contained in this document are those of the authors and should not be interpreted as representing the official policies, either expressed or implied, of the Army Research Office or the U.S. Government. The authors thank Michael Faran for fruitful discussions.

Supporting Information Available

The Supporting Information includes detailed sections on the implementation of square wave potential in nonequilibrium MD simulations, comparative dynamics of self-assembly in patchy particle systems, the influence of patch length on self-assembly kinetics and stability, the impact of number density on self-assembly, and the sustained order parameter in nonequilibrium dynamics, featuring:

Fig. S1: Order Parameter (R) and total Entropy Production (S) dynamics for 8-patchy particles under external drive. **Fig. S2:** Order Parameter (R) and total Entropy Production (S) variations in 13-patchy particles, showing drive and energy effects. **Fig. S3:** Total Entropy Production (S) and order Parameter (R) variations in 8-patchy particles in equilibrium and nonequilibrium for successful realization of the target. **Fig. S4:** T_{fas} and T_{stable} changes with patch energy and drive in 10-patch systems under different patch lengths. **Fig. S5:** Impact of number density on T_{fas} and T_{stable} in 10-patch systems under different conditions. **Fig. S6:** Consistent R growth in 8-patch and 10-patch systems across square wave potential amplitudes. **Fig. S7:** Average number of bond formation and dissociation events. **Fig. S8:** Variation of N_B as a function of MC steps for 100 particles with 8-ring

specification with and without external drive. **Fig. S9:** Variation of N_B and N_R as a function of MC steps for 100 particles with 4-ring specification with and without external drive. **Fig. S10:** Variation of N_B as a function of MC steps for 100 particles with 8-ring specification in equilibrium.

A series of supplementary movies illustrate the dynamic behavior of the systems: **Movie S1:** Equilibrium MC, 8 particles, 2 state. **Movie S2:** Equilibrium MC, 10 particles, 2 states. **Movie S3:** Equilibrium MC, 13 particles, 2 state. **Movie S4:** Nonequilibrium MC, 8 particles, 2 states. **Movie S5:** Nonequilibrium MC, 10 particles, 2 states. **Movie S6:** Nonequilibrium MC, 13 particles, 2 states. **Movie S7:** Equilibrium MD, 8 particles, 1 state. **Movie S8:** Equilibrium MD, 10 particles, 1 states. **Movie S9:** Nonequilibrium MD, 8 particles, 1 state. **Movie S10:** Nonequilibrium MD, 10 particles, 1 states. **Movie S11:** Equilibrium MC, 100 particles, 1 state, 8-ring specification. **Movie S12:** Equilibrium MC, 100 particles, 1 state, 4-ring specification.

References

- (1) Whitesides, G. M.; Grzybowski, B. Self-Assembly at All Scales. *Science* **2002**, *295*, 2418–2421.
- (2) Reinhardt, A.; Frenkel, D. DNA brick self-assembly with an off-lattice potential. *Soft Matter* **2016**, *12*, 6253–6260.
- (3) Moaseri, E.; Bollinger, J. A.; Changalvaie, B.; Johnson, L.; Schroer, J.; Johnston, K. P.; Truskett, T. M. Reversible Self-Assembly of Glutathione-Coated Gold Nanoparticle Clusters via pH-Tunable Interactions. *Langmuir* **2017**, *33*, 12244–12253.
- (4) Jadrich, R. B.; Lindquist, B. A.; Truskett, T. M. Probabilistic inverse design for self-assembling materials. *The Journal of Chemical Physics* **2017**, *146*, 184103.
- (5) Cumberworth, A.; Reinhardt, A.; Frenkel, D. Lattice models and Monte Carlo methods

- for simulating DNA origami self-assembly. *The Journal of Chemical Physics* **2018**, *149*, 234905.
- (6) Liu, D.; Aleisa, R.; Cai, Z.; Li, Y.; Yin, Y. Self-assembly of superstructures at all scales. *Matter* **2021**, *4*, 927–941.
- (7) Bassani, C. L. et al. Nanocrystal Assemblies: Current Advances and Open Problems. *ACS Nano* **2024**,
- (8) Gao, W.; Hu, C.-M. J.; Fang, R. H.; Zhang, L. Liposome-like nanostructures for drug delivery. *J. Mater. Chem. B* **2013**, *1*, 6569–6585.
- (9) Verma, G.; Hassan, P. A. Self assembled materials: design strategies and drug delivery perspectives. *Phys. Chem. Chem. Phys.* **2013**, *15*, 17016–17028.
- (10) Filipczak, N.; Pan, J.; Yalamarty, S. S. K.; Torchilin, V. P. Recent advancements in liposome technology. *Advanced Drug Delivery Reviews* **2020**, *156*, 4–22.
- (11) Shaw, C. P.; Fernig, D. G.; Lévy, R. Gold nanoparticles as advanced building blocks for nanoscale self-assembled systems. *J. Mater. Chem.* **2011**, *21*, 12181–12187.
- (12) Yang, G.; Nanda, J.; Wang, B.; Chen, G.; Hallinan, D. T. J. Self-Assembly of Large Gold Nanoparticles for Surface-Enhanced Raman Spectroscopy. *ACS Applied Materials & Interfaces* **2017**, *9*, 13457–13470.
- (13) Bian, K.; Schunk, H.; Ye, D.; Hwang, A.; Luk, T. S.; Li, R.; Wang, Z.; Fan, H. Formation of self-assembled gold nanoparticle supercrystals with facet-dependent surface plasmonic coupling. *Nature Communications* **2018**, *9*, 2365.
- (14) Fialkowski, M.; Bishop, K. J. M.; Klajn, R.; Smoukov, S. K.; Campbell, C. J.; Grzybowski, B. A. Principles and Implementations of Dissipative (Dynamic) Self-Assembly. *The Journal of Physical Chemistry B* **2006**, *110*, 2482–2496.

- (15) England, J. L. Dissipative adaptation in driven self-assembly. *Nature Nanotechnology* **2015**, *10*, 919–923.
- (16) Bisker, G. Dissipate your way to self-assembly. *Nature Physics* **2020**, *16*, 707–708.
- (17) Makey, G.; Galioglu, S.; Ghaffari, R.; Engin, E. D.; Yıldırım, G.; Yavuz, Ö.; Bektaş, O.; Nizam, Ü. S.; Akbulut, Ö.; Şahin, Ö.; Güngör, K.; Dede, D.; Demir, H. V.; Ilday, F. Ö.; Ilday, S. Universality of dissipative self-assembly from quantum dots to human cells. *Nature Physics* **2020**, *16*, 795–801.
- (18) Liu, J. et al. Light-Induced Self-Assembly of Cubic CsPbBr₃ Perovskite Nanocrystals into Nanowires. *Chemistry of Materials* **2019**, *31*, 6642–6649.
- (19) Cheng, M.; Chen, D.; Zhang, L.; Xiao, T.; Jiang, J.; Wang, L. Chemical fuel-driven gelation with dissipative assembly-induced emission. *Org. Chem. Front.* **2023**, *10*, 1380–1385.
- (20) Grötsch, R. K.; Wanzke, C.; Speckbacher, M.; Angı, A.; Rieger, B.; Boekhoven, J. Pathway Dependence in the Fuel-Driven Dissipative Self-Assembly of Nanoparticles. *Journal of the American Chemical Society* **2019**, *141*, 9872–9878.
- (21) Wiewiórski, P.; Streck, W.; Tomala, R.; Stefanski, M. Electric field driven self-assembly of dissolved graphene foam particles in a capillary. *Materials Letters* **2023**, *335*, 133851.
- (22) Park, M.; Kang, S.; Nam, C.; Narasimha, K.; Lee, W. B.; Park, S.-J. Magnetic Field-Induced Self-Assembly of Conjugated Block Copolymers and Nanoparticles at the Air–Water Interface. *ACS Applied Materials & Interfaces* **2022**, *14*, 8266–8273.
- (23) Prigogine, I. *Introduction to Thermodynamics of Irreversible Processes*; Wiley, 1978; pp 1–147.

- (24) Marsland, R.; England, J. Far-from-equilibrium distribution from near-steady-state work fluctuations. *Phys. Rev. E* **2015**, *92*, 052120.
- (25) Marsland, R.; England, J. Limits of predictions in thermodynamic systems: a review. *Reports on Progress in Physics* **2017**, *81*, 016601.
- (26) Nguyen, M.; Qiu, Y.; Vaikuntanathan, S. Organization and Self-Assembly Away from Equilibrium: Toward Thermodynamic Design Principles. *Annual Review of Condensed Matter Physics* **2021**, *12*, 273–290.
- (27) Chvykov, P.; Berrueta, T. A.; Vardhan, A.; Savoie, W.; Samland, A.; Murphey, T. D.; Wiesenfeld, K.; Goldman, D. I.; England, J. L. Low rattling: A predictive principle for self-organization in active collectives. *Science* **2021**, *371*, 90–95.
- (28) England, J. L. Self-organized computation in the far-from-equilibrium cell. *Biophysics Reviews* **2022**, *3*, 041303.
- (29) Penocchio, E.; Rao, R.; Esposito, M. Thermodynamic efficiency in dissipative chemistry. *Nature Communications* **2019**, *10*, 3865.
- (30) Tociu, L.; Fodor, E.; Nemoto, T.; Vaikuntanathan, S. How Dissipation Constrains Fluctuations in Nonequilibrium Liquids: Diffusion, Structure, and Biased Interactions. *Phys. Rev. X* **2019**, *9*, 041026.
- (31) Penocchio, E.; Rao, R.; Esposito, M. Nonequilibrium thermodynamics of light-induced reactions. *The Journal of Chemical Physics* **2021**, *155*, 114101.
- (32) Korbelt, J.; Lindner, S. D.; Hanel, R.; Thurner, S. Thermodynamics of structure-forming systems. *Nature Communications* **2021**, *12*, 1127.
- (33) Trubiano, A.; Holmes-Cerfon, M. Thermodynamic stability versus kinetic accessibility: Pareto fronts for programmable self-assembly. *Soft Matter* **2021**, *17*, 6797–6807.

- (34) Gartner, F. M.; Graf, I. R.; Frey, E. The time complexity of self-assembly. *Proceedings of the National Academy of Sciences* **2022**, *119*, e2116373119.
- (35) Gartner, F. M.; Frey, E. Design Principles for Fast and Efficient Self-Assembly Processes. *Phys. Rev. X* **2024**, *14*, 021004.
- (36) Hagan, M. F.; Elrad, O. M.; Jack, R. L. Mechanisms of kinetic trapping in self-assembly and phase transformation. *The Journal of Chemical Physics* **2011**, *135*, 104115.
- (37) Michaels, T. C. T.; Bellaiche, M. M. J.; Hagan, M. F.; Knowles, T. P. J. Kinetic constraints on self-assembly into closed supramolecular structures. *Scientific Reports* **2017**, *7*, 12295.
- (38) Murugan, A.; Zeravcic, Z.; Brenner, M. P.; Leibler, S. Multifarious assembly mixtures: Systems allowing retrieval of diverse stored structures. *Proceedings of the National Academy of Sciences* **2015**, *112*, 54–59.
- (39) Osat, S.; Golestanian, R. Non-reciprocal multifarious self-organization. *Nature Nanotechnology* **2023**, *18*, 79–85.
- (40) Osat, S.; Metson, J.; Kardar, M.; Golestanian, R. Escaping kinetic traps using non-reciprocal interactions. *arXiv preprint arXiv:2309.00562* **2023**,
- (41) Boekhoven, J.; Brizard, A. M.; Kowligi, K. N. K.; Koper, G. J. M.; Eelkema, R.; van Esch, J. H. Dissipative Self-Assembly of a Molecular Gelator by Using a Chemical Fuel. *Angewandte Chemie International Edition* **2010**, *49*, 4825–4828.
- (42) Koper, G. J. M.; Boekhoven, J.; Hendriksen, W. E.; van Esch, J. H.; Eelkema, R.; Pagonabarraga, I.; Rubí, J. M.; Bedeaux, D. The Lost Work in Dissipative Self-Assembly. *International Journal of Thermophysics* **2013**, *34*, 1229–1238.

- (43) England, J. L. Statistical physics of self-replication. *The Journal of Chemical Physics* **2013**, *139*, 121923.
- (44) Kedia, H.; Pan, D.; Slotine, J.-J.; England, J. L. Drive-specific selection in multistable mechanical networks. *The Journal of Chemical Physics* **2023**, *159*, 214106.
- (45) Subramani, K.; Ahmed, W. In *Emerging Nanotechnologies in Dentistry (Second Edition)*, second edition ed.; Subramani, K., Ahmed, W., Eds.; Micro and Nano Technologies; William Andrew Publishing, 2018; pp 231–249.
- (46) Sartori, P.; Leibler, S. Lessons from equilibrium statistical physics regarding the assembly of protein complexes. *Proceedings of the National Academy of Sciences* **2020**, *117*, 114–120.
- (47) Vale, R.; Coppin, C.; Malik, F.; Kull, F.; Milligan, R. Tubulin GTP hydrolysis influences the structure, mechanical properties, and kinesin-driven transport of microtubules. *Journal of Biological Chemistry* **1994**, *269*, 23769–23775.
- (48) Mayer, M. P.; Bukau, B. Hsp70 chaperones: Cellular functions and molecular mechanism. *Cellular and Molecular Life Sciences* **2005**, *62*, 670.
- (49) Goloubinoff, P.; Sassi, A. S.; Fauvet, B.; Barducci, A.; De Los Rios, P. Chaperones convert the energy from ATP into the nonequilibrium stabilization of native proteins. *Nature Chemical Biology* **2018**, *14*, 388–395.
- (50) Fletcher, D. A.; Mullins, R. D. Cell mechanics and the cytoskeleton. *Nature* **2010**, *463*, 485–492.
- (51) Vöpel, T.; Syguda, A.; Britzen-Laurent, N.; Kunzelmann, S.; Lüdemann, M.-B.; Dovengerds, C.; Stürzl, M.; Herrmann, C. Mechanism of GTPase-Activity-Induced Self-Assembly of Human Guanylate Binding Protein 1. *Journal of Molecular Biology* **2010**, *400*, 63–70.

- (52) Deng, J.; Walther, A. ATP-Responsive and ATP-Fueled Self-Assembling Systems and Materials. *Advanced Materials* **2020**, *32*, 2002629.
- (53) Ma, W.; Zhan, Y.; Zhang, Y.; Mao, C.; Xie, X.; Lin, Y. The biological applications of DNA nanomaterials: current challenges and future directions. *Signal Transduction and Targeted Therapy* **2021**, *6*, 351.
- (54) Dzieciol, A. J.; Mann, S. Designs for life: protocell models in the laboratory. *Chem. Soc. Rev.* **2012**, *41*, 79–85.
- (55) Cheng, C.; McGonigal, P. R.; Stoddart, J. F.; Astumian, R. D. Design and Synthesis of Nonequilibrium Systems. *ACS Nano* **2015**, *9*, 8672–8688.
- (56) Pezzato, C.; Cheng, C.; Stoddart, J. F.; Astumian, R. D. Mastering the non-equilibrium assembly and operation of molecular machines. *Chem. Soc. Rev.* **2017**, *46*, 5491–5507.
- (57) Rao, A.; Roy, S.; Jain, V.; Pillai, P. P. Nanoparticle Self-Assembly: From Design Principles to Complex Matter to Functional Materials. *ACS Applied Materials & Interfaces* **2023**, *15*, 25248–25274.
- (58) Bechstedt, S.; Brouhard, G. J. Doublecortin Recognizes the 13-Protofilament Microtubule Cooperatively and Tracks Microtubule Ends. *Developmental Cell* **2012**, *23*, 181–192.
- (59) Insua, I.; Montenegro, J. 1D to 2D Self Assembly of Cyclic Peptides. *Journal of the American Chemical Society* **2020**, *142*, 300–307.
- (60) Zhao, Y.; Yu, L.; Zhang, S.; Su, X.; Zhou, X. Extrachromosomal circular DNA: Current status and future prospects. **2022**, *11*, e81412.
- (61) Cabezón, A.; Calvelo, M.; Granja, J. R.; Piñeiro, Á.; Garcia-Fandino, R. Uncovering

- the mechanisms of cyclic peptide self-assembly in membranes with the chirality-aware MA(R/S)TINI forcefield. *Journal of Colloid and Interface Science* **2023**, *642*, 84–99.
- (62) Li, Q.; So, C. R.; Fegan, A.; Cody, V.; Sarikaya, M.; Vallera, D. A.; Wagner, C. R. Chemically Self-Assembled Antibody Nanorings (CSANs): Design and Characterization of an Anti-CD3 IgM Biomimetic. *Journal of the American Chemical Society* **2010**, *132*, 17247–17257.
- (63) Mews, E. A.; Beckmann, P.; Patchava, M.; Wang, Y.; Largaespada, D. A.; Wagner, C. R. Multivalent, Bispecific α B7-H3- α CD3 Chemically Self-Assembled Nanorings Direct Potent T Cell Responses against Medulloblastoma. *ACS Nano* **2022**, *16*, 12185–12201.
- (64) Dunn, K. E.; Elfick, A. Harnessing DNA Nanotechnology and Chemistry for Applications in Photonics and Electronics. *Bioconjugate Chemistry* **2023**, *34*, 97–104.
- (65) Li, W.; Palis, H.; Mérindol, R.; Majimel, J.; Ravaine, S.; Duguet, E. Colloidal molecules and patchy particles: complementary concepts, synthesis and self-assembly. *Chem. Soc. Rev.* **2020**, *49*, 1955–1976.
- (66) Boltzmann, L. *Lectures on Gas Theory*; Dover: New York, NY, 1905; pp 339–371.
- (67) Casagrande, C.; Fabre, P.; Raphaël, E.; Veyssié, M. “Janus Beads”: Realization and Behaviour at Water/Oil Interfaces. *Europhysics Letters* **1989**, *9*, 251.
- (68) Zhang, Z.; Glotzer, S. C. Self-Assembly of Patchy Particles. *Nano Letters* **2004**, *4*, 1407–1413.
- (69) Hong, L.; Jiang, S.; Granick, S. Simple Method to Produce Janus Colloidal Particles in Large Quantity. *Langmuir* **2006**, *22*, 9495–9499.
- (70) Pawar, A. B.; Kretzschmar, I. Multifunctional Patchy Particles by Glancing Angle Deposition. *Langmuir* **2009**, *25*, 9057–9063.

- (71) Gong, Z.; Hueckel, T.; Yi, G.-R.; Sacanna, S. Patchy particles made by colloidal fusion. *Nature* **2017**, *550*, 234–238.
- (72) Lotierzo, A.; Longbottom, B. W.; Lee, W. H.; Bon, S. A. F. Synthesis of Janus and Patchy Particles Using Nanogels as Stabilizers in Emulsion Polymerization. *ACS Nano* **2019**, *13*, 399–407.
- (73) Paul, S.; Vashisth, H. Self-assembly behavior of experimentally realizable lobed patchy particles. *Soft Matter* **2020**, *16*, 8101–8107.
- (74) Virk, M. M.; Beitzl, K. N.; van Oostrum, P. D. J. Synthesis of patchy particles using gaseous ligands. *Journal of Physics: Condensed Matter* **2023**, *35*, 174003.
- (75) Shah, A. A.; Schultz, B.; Kohlstedt, K. L.; Glotzer, S. C.; Solomon, M. J. Synthesis, Assembly, and Image Analysis of Spheroidal Patchy Particles. *Langmuir* **2013**, *29*, 4688–4696.
- (76) Chang, F.; Ouahjji, S.; Townsend, A.; Sanogo Lacina, K.; van Ravensteijn, B. G.; Kegel, W. K. Controllable synthesis of patchy particles with tunable geometry and orthogonal chemistry. *Journal of Colloid and Interface Science* **2021**, *582*, 333–341.
- (77) Langer, R.; Tirrell, D. A. Designing materials for biology and medicine. *Nature* **2004**, *428*, 487–492.
- (78) Wong, C. K.; Chen, F.; Walther, A.; Stenzel, M. H. Bioactive Patchy Nanoparticles with Compartmentalized Cargoes for Simultaneous and Trackable Delivery. *Angewandte Chemie International Edition* **2019**, *58*, 7335–7340.
- (79) Liddell, C.; Summers, C.; Gokhale, A. Stereological estimation of the morphology distribution of ZnS clusters for photonic crystal applications. *Materials Characterization* **2003**, *50*, 69–79.

- (80) Rao, A. B.; Shaw, J.; Neophytou, A.; Morpew, D.; Sciortino, F.; Johnston, R. L.; Chakrabarti, D. Leveraging Hierarchical Self-Assembly Pathways for Realizing Colloidal Photonic Crystals. *ACS Nano* **2020**, *14*, 5348–5359.
- (81) Cai, Z.; Li, Z.; Ravaine, S.; He, M.; Song, Y.; Yin, Y.; Zheng, H.; Teng, J.; Zhang, A. From colloidal particles to photonic crystals: advances in self-assembly and their emerging applications. *Chem. Soc. Rev.* **2021**, *50*, 5898–5951.
- (82) Flavell, W.; Neophytou, A.; Demetriadou, A.; Albrecht, T.; Chakrabarti, D. Programmed Self-Assembly of Single Colloidal Gyroids for Chiral Photonic Crystals. *Advanced Materials* **2023**, *35*, 2211197.
- (83) Pawar, A. B.; Kretzschmar, I. Fabrication, Assembly, and Application of Patchy Particles. *Macromolecular Rapid Communications* **2010**, *31*, 150–168.
- (84) Song, P.; Wang, Y.; Wang, Y.; Hollingsworth, A. D.; Weck, M.; Pine, D. J.; Ward, M. D. Patchy Particle Packing under Electric Fields. *Journal of the American Chemical Society* **2015**, *137*, 3069–3075.
- (85) Shields IV, C. W.; Zhu, S.; Yang, Y.; Bharti, B.; Liu, J.; Yellen, B. B.; Velev, O. D.; López, G. P. Field-directed assembly of patchy anisotropic microparticles with defined shape. *Soft Matter* **2013**, *9*, 9219–9229.
- (86) Nguemaha, V.; Zhou, H.-X. Liquid-Liquid Phase Separation of Patchy Particles Illuminates Diverse Effects of Regulatory Components on Protein Droplet Formation. *Scientific Reports* **2018**, *8*, 6728.
- (87) Gnan, N.; Sciortino, F.; Zaccarelli, E. In *Protein Self-Assembly: Methods and Protocols*; McManus, J. J., Ed.; Springer New York: New York, NY, 2019; pp 187–208.
- (88) Neophytou, A.; Chakrabarti, D.; Sciortino, F. Facile self-assembly of colloidal dia-

- mond from tetrahedral patchy particles via ring selection. *Proceedings of the National Academy of Sciences* **2021**, *118*, e2109776118.
- (89) Beneduce, C.; E. P. Pinto, D.; Šulc, P.; Sciortino, F.; Russo, J. Two-step nucleation in a binary mixture of patchy particles. *The Journal of Chemical Physics* **2023**, *158*, 154502.
- (90) McMullen, A.; Holmes-Cerfon, M.; Sciortino, F.; Grosberg, A. Y.; Brujic, J. Freely Jointed Polymers Made of Droplets. *Phys. Rev. Lett.* **2018**, *121*, 138002.
- (91) Doye, J. P. K.; Louis, A. A.; Lin, I.-C.; Allen, L. R.; Noya, E. G.; Wilber, A. W.; Kok, H. C.; Lyus, R. Controlling crystallization and its absence: proteins, colloids and patchy models. *Phys. Chem. Chem. Phys.* **2007**, *9*, 2197–2205.
- (92) Noya, E. G.; Vega, C.; Doye, J. P. K.; Louis, A. A. The stability of a crystal with diamond structure for patchy particles with tetrahedral symmetry. *The Journal of Chemical Physics* **2010**, *132*, 234511.
- (93) Tracey, D. F.; Noya, E. G.; Doye, J. P. K. Programming patchy particles to form three-dimensional dodecagonal quasicrystals. *The Journal of Chemical Physics* **2021**, *154*, 194505.
- (94) Bianchi, E.; Largo, J.; Tartaglia, P.; Zaccarelli, E.; Sciortino, F. Phase Diagram of Patchy Colloids: Towards Empty Liquids. *Phys. Rev. Lett.* **2006**, *97*, 168301.
- (95) Espinosa, J. R.; Garaizar, A.; Vega, C.; Frenkel, D.; Collepardo-Guevara, R. Breakdown of the law of rectilinear diameter and related surprises in the liquid-vapor coexistence in systems of patchy particles. *The Journal of Chemical Physics* **2019**, *150*, 224510.
- (96) Bisker, G.; England, J. L. Nonequilibrium associative retrieval of multiple stored self-

- assembly targets. *Proceedings of the National Academy of Sciences* **2018**, *115*, E10531–E10538.
- (97) Zhou, J.; Wang, A.; Song, Y.; Liu, N.; Wang, J.; Li, Y.; Liang, X.; Li, G.; Chu, H.; Wang, H.-W. Structural insights into the mechanism of GTP initiation of microtubule assembly. *Nature Communications* **2023**, *14*, 5980.
- (98) Ben-Ari, A.; Ben-Ari, L.; Bisker, G. Nonequilibrium self-assembly of multiple stored targets in a dimer-based system. *The Journal of Chemical Physics* **2021**, *155*, 234113.
- (99) Faran, M.; Bisker, G. Nonequilibrium Self-Assembly Time Forecasting by the Stochastic Landscape Method. *The Journal of Physical Chemistry B* **2023**, *127*, 6113–6124.
- (100) Faran, M.; Ray, D.; Nag, S.; Raucchi, U.; Parrinello, M.; Bisker, G. A Stochastic Landscape Approach for Protein Folding State Classification. *Journal of Chemical Theory and Computation* **2024**, *20*, 5428–5438.
- (101) Heinonen, J. K. *Biological Role of Inorganic Pyrophosphate*; Springer New York, NY: New York, NY, 2012; pp 1–250.
- (102) Rovigatti, L.; Russo, J.; Romano, F. How to simulate patchy particles. *The European Physical Journal E* **2018**, *41*, 59.
- (103) Kern, N.; Frenkel, D. Fluid–fluid coexistence in colloidal systems with short-ranged strongly directional attraction. *The Journal of Chemical Physics* **2003**, *118*, 9882–9889.
- (104) Zhang; Keys, A. S.; Chen, T.; Glotzer, S. C. Self-Assembly of Patchy Particles into Diamond Structures through Molecular Mimicry. *Langmuir* **2005**, *21*, 11547–11551.
- (105) Newton, A. C.; Groenewold, J.; Kegel, W. K.; Bolhuis, P. G. Rotational diffusion affects the dynamical self-assembly pathways of patchy particles. *Proceedings of the National Academy of Sciences* **2015**, *112*, 15308–15313.

- (106) Reinhart, W. F.; Panagiotopoulos, A. Z. Equilibrium crystal phases of triblock Janus colloids. *The Journal of Chemical Physics* **2016**, *145*, 094505.
- (107) Jonas, H. J.; Stuij, S. G.; Schall, P.; Bolhuis, P. G. A temperature-dependent critical Casimir patchy particle model benchmarked onto experiment. *The Journal of Chemical Physics* **2021**, *155*, 034902.
- (108) Smallenburg, F.; Sciortino, F. Liquids more stable than crystals in particles with limited valence and flexible bonds. *Nature Physics* **2013**, *9*, 554–558.
- (109) Metropolis, N.; Rosenbluth, A. W.; Rosenbluth, M. N.; Teller, A. H.; Teller, E. Equation of State Calculations by Fast Computing Machines. *The Journal of Chemical Physics* **1953**, *21*, 1087–1092.
- (110) Mariottini, D.; Del Giudice, D.; Ercolani, G.; Di Stefano, S.; Ricci, F. Dissipative operation of pH-responsive DNA-based nanodevices. *Chem. Sci.* **2021**, *12*, 11735–11739.
- (111) Mazzotti, G.; Hartmann, D.; Booth, M. J. Precise, Orthogonal Remote-Control of Cell-Free Systems Using Photocaged Nucleic Acids. *Journal of the American Chemical Society* **2023**, *145*, 9481–9487.
- (112) Berg, W. R.; Berengut, J. F.; Bai, C.; Wimberger, L.; Lee, L. K.; Rizzuto, F. J. Light-Activated Assembly of DNA Origami into Dissipative Fibrils. *Angewandte Chemie International Edition* **2023**, *62*, e202314458.
- (113) Byrom, J.; Biswal, S. L. Magnetic field directed assembly of two-dimensional fractal colloidal aggregates. *Soft Matter* **2013**, *9*, 9167–9173.
- (114) Thompson, A. P.; Aktulga, H. M.; Berger, R.; Bolintineanu, D. S.; Brown, W. M.; Crozier, P. S.; in 't Veld, P. J.; Kohlmeyer, A.; Moore, S. G.; Nguyen, T. D.; Shan, R.;

- Stevens, M. J.; Tranchida, J.; Trott, C.; Plimpton, S. J. LAMMPS - a flexible simulation tool for particle-based materials modeling at the atomic, meso, and continuum scales. *Computer Physics Communications* **2022**, *271*, 108171.
- (115) Jover, J.; Haslam, A. J.; Galindo, A.; Jackson, G.; Müller, E. A. Pseudo hard-sphere potential for use in continuous molecular-dynamics simulation of spherical and chain molecules. *The Journal of Chemical Physics* **2012**, *137*, 144505.
- (116) Espinosa, J. R.; Vega, C.; Sanz, E. The mold integration method for the calculation of the crystal-fluid interfacial free energy from simulations. *The Journal of Chemical Physics* **2014**, *141*, 134709.
- (117) Nosé, S. A unified formulation of the constant temperature molecular dynamics methods. *The Journal of Chemical Physics* **1984**, *81*, 511–519.
- (118) Hoover, W. G. Canonical dynamics: Equilibrium phase-space distributions. *Phys. Rev. A* **1985**, *31*, 1695–1697.
- (119) Swope, W. C.; Andersen, H. C.; Berens, P. H.; Wilson, K. R. A computer simulation method for the calculation of equilibrium constants for the formation of physical clusters of molecules: Application to small water clusters. *The Journal of Chemical Physics* **1982**, *76*, 637–649.
- (120) Terlau, H.; Stühmer, W. Structure and Function of Voltage-Gated Ion Channels. *Naturwissenschaften* **1998**, *85*, 437–444.
- (121) Fang, X.; Liu, Q.; Bohrer, C.; Hensel, Z.; Han, W.; Wang, J.; Xiao, J. Cell fate potentials and switching kinetics uncovered in a classic bistable genetic switch. *Nature Communications* **2018**, *9*, 2787.
- (122) Seifert, U. Stochastic thermodynamics, fluctuation theorems and molecular machines. *Reports on Progress in Physics* **2012**, *75*, 126001.

- (123) Nag, S.; Bisker, G. Driven Self-Assembly of Patchy Particles through Monte Carlo and Molecular Dynamics Simulations. *10.1021/acs.jctc.4c01118*
- (124) Sato, M. Effect of Patch Area and Interaction Length on Clusters and Structures Formed by One-Patch Particles in Thin Systems. *ACS Omega* **2020**, *5*, 28812–28822.
- (125) Klein, H. C. R.; Schwarz, U. S. Studying protein assembly with reversible Brownian dynamics of patchy particles. *The Journal of Chemical Physics* **2014**, *140*, 184112.
- (126) Michaels, T. C.; Feng, S.; Liang, H.; Mahadevan, L. Mechanics and kinetics of dynamic instability. *eLife* **2020**, *9*, e54077.

Supporting Information:

**Dissipative self-assembly of patchy particles
under nonequilibrium drive: a computational
study**

Shubhadeep Nag[†] and Gili Bisker^{*,†,‡,¶,§,||}

[†]*Department of Biomedical Engineering, Faculty of Engineering, Tel Aviv University, Tel Aviv 69978, Israel*

[‡]*The Center for Physics and Chemistry of Living Systems, Tel Aviv University, Tel Aviv 6997801, Israel*

[¶]*The Center for Nanoscience and Nanotechnology, Tel Aviv University, Tel Aviv 6997801, Israel*

[§]*The Center for Light-Matter Interaction, Tel Aviv University, Tel Aviv 6997801, Israel*

^{||}*The Center for Computational Molecular and Materials Science, Tel Aviv University, Tel Aviv 6997801, Israel*

E-mail: bisker@tauex.tau.ac.il

S1 Total Entropy Production Calculation in MC Simulations

The calculation of entropy production in MC simulations involves summing the contributions from each accepted MC move, where each move alters the system's energy. The contribution is calculated by k_B times the log-ratio of the forward and reverse transition probabilities.¹ Let $P_{forward}$ be the probability of moving forward from one state to another, and $P_{reverse}$ be the probability of moving reverse between the same two states.

During an MC step, if a particle transitions from an initial energy (E_{ini}) to a final energy (E_{final}), the energy change ($\delta E = E_{final} - E_{ini}$) determines the transition probabilities. If $\delta E < 0$, indicating a decrease in energy, the forward transition probability, $P_{forward}$, is 1 and the reverse transition probability, $P_{reverse}$, is $e^{+\delta E/k_B T}$, T is the temperature. Conversely, if $\delta E > 0$, signifying an increase in energy, the forward transition probability, $P_{forward}$, is $e^{-\delta E/k_B T}$, and the reverse transition probability, $P_{reverse}$, is 1. Thus, the contribution to entropy production, namely $k_B \ln(\frac{P_{forward}}{P_{reverse}})$, in the case of $\delta E > 0$ is $-\frac{\delta E}{T}$, and in the opposite case, $\delta E < 0$, it is $+\frac{\delta E}{T}$. In MC simulations, entropy production accumulates from these probabilistic energy changes and sums to the total entropy change over the course of the simulation. The total entropy production, S is the sum of these contributions. The resulting total entropy production is in the units of the (molar) energy divided by the temperature, kJ / (mol · K).

S2 Self-Assembly Dynamics in 8 and 13 patchy Particle Systems in MC Simulations

We extend the analysis of the order parameter, R , and the total entropy production, S , to systems of 8 and 13 patchy particles, in addition to the 10 patchy particle system presented in the main text.

The evolution of R for a 8 patchy particle system under equilibrium ($\epsilon_{drive} = 0$) and nonequilibrium ($\epsilon_{drive} = 5$ kJ/mol) conditions is depicted in Fig. S1(a) and Fig. S1(b), respectively, for a patchy interaction value $\epsilon_{patch} = 4$ kJ/mol. In the absence of an external drive, R displays stochastic behavior, oscillating between 0 (i.e., no bond formed) and 0.75 (i.e., 6 bonds formed out of the 8 possible bonds), indicating the inability of the system to self-assemble the target structure. With the external drive, R displays a rapid transition from a disordered state to the fully assembled target, corresponding to $R = 1$ at 1.3×10^6 MC steps. The total entropy production, S , without the drive, shows zero entropy production rate (Fig. S1(c)), in contrast to the nonequilibrium case where the value of S rapidly increases (Fig. S1(d)), reflecting the energy dissipation associated with the use of the external drive.

Similarly, for the 13 patchy particle system with $\epsilon_{patch} = 5$ kJ/mol, R fluctuates randomly only between 0.4 and 0.8 through the entire course of the simulation under equilibrium conditions (Fig. S2(a)), where under nonequilibrium conditions with $\epsilon_{drive} = 7$ kJ/mol, R increases in a step-wise manner until it reaches the value of 1 at 3.9×10^6 MC steps for the first time, which represents a fully assembled structure (Fig. S2(b)). Moreover, S displays fluctuations with mean zero graduate, indicating zero entropy production rate at equilibrium (Fig. S2(c)), whereas with the external drive, S rapidly increases (Fig. S2(d)).

These results demonstrate that external driving forces not only facilitate the self-assembly of patchy particles into a predefined structure but also modulate the thermodynamic signatures of the process. This modulation is evident in the transition to an ordered state captured by the increase in R and S . Furthermore, to provide a comparison, the computation of S and R for both equilibrium and nonequilibrium cases, where each realization reaches the target structure, is plotted in Fig. S3.

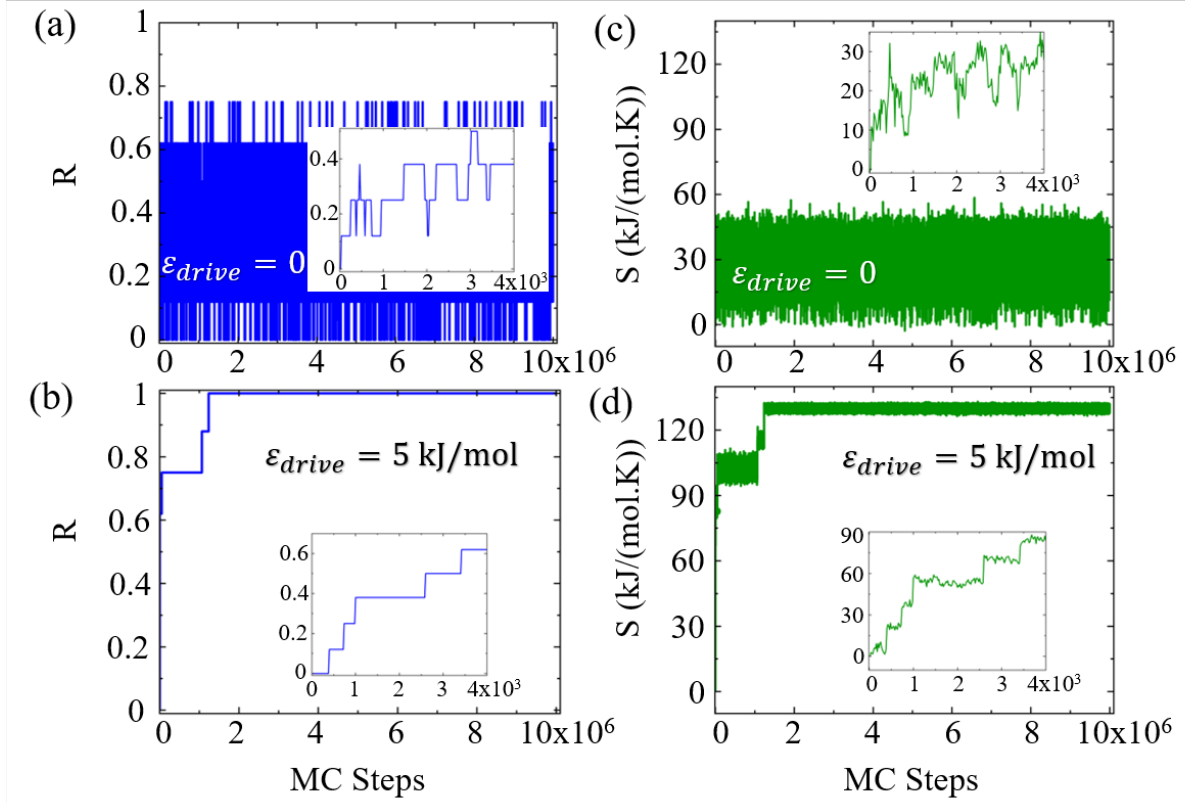


Figure S1: Results of 8 patchy particle system. Order parameter (R) as a function of MC steps (a) in equilibrium and (b) under nonequilibrium conditions with an external drive $\epsilon_{drive} = 5$ kJ/mol. The total entropy production (S) as a function of MC steps (c) in equilibrium and (d) under nonequilibrium conditions with an external drive $\epsilon_{drive} = 5$ kJ/mol. Results are presented for a single MC realization with $\epsilon_{patch} = 4$ kJ/mol. The inset plots show Zoom in into the early simulation steps.

S3 Effect of Patch Length on Self-Assembly Kinetics in MC Simulations

In addition to the the patch length chosen for our main analysis, 0.85 \AA , we extend our simulations to include patch lengths of 0.4 \AA and 1.1 \AA to investigate the effect of this parameter on the results for the 10 patchy particle system. Under equilibrium conditions, both the median self-assembly time, T_{fas} (Fig. S4(a)), and median stability time, T_{stable} (Fig. S4(b)), show a similar trend as a function of the patch interaction energy, ϵ_{patch} , for the 3 patch length values tested.

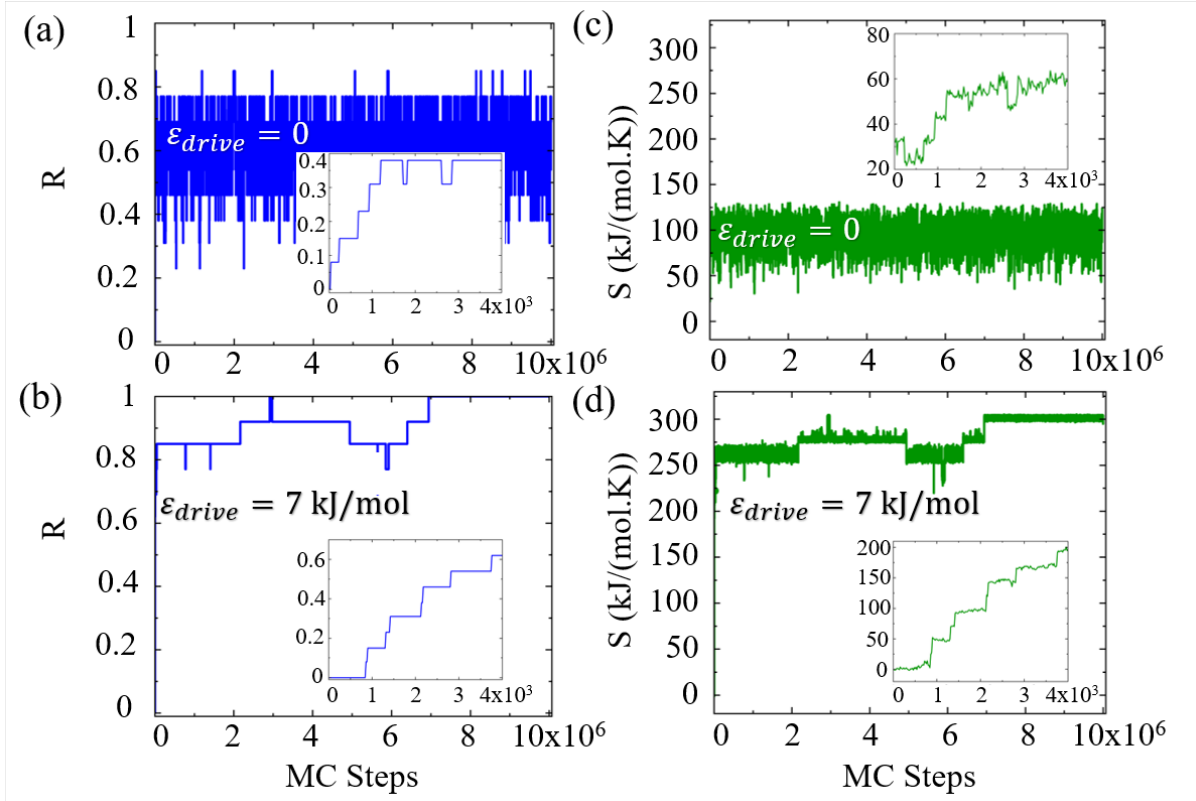


Figure S2: Results of 13 patchy particle system. Order parameter (R) as a function of MC steps (a) in equilibrium and (b) under nonequilibrium conditions with an external drive $\epsilon_{drive} = 7$ kJ/mol. The total entropy production (S) as a function of MC steps (c) in equilibrium and (d) under nonequilibrium conditions with an external drive $\epsilon_{drive} = 7$ kJ/mol. Results are presented for a single MC realization with $\epsilon_{patch} = 5$ kJ/mol.

Under nonequilibrium conditions, with $\epsilon_{patch} = 5$ kJ/mol, we also observe a similar trend of T_{fas} (Fig. S4(c)) and T_{stable} (Fig. S4(d)), showing faster assembly and higher stability, respectively, for increasing drive value ϵ_{drive} , for the various patch lengths. These results confirm that our conclusions hold irrespective of the chosen patch length parameter value.

S4 Effect of Simulation Cell Dimension on Self-Assembly Kinetics in MC Simulations

Understanding the kinetics of self-assembly in the context of number density is important for tuning the properties of assembled structures. In addition to the simulation cell length of

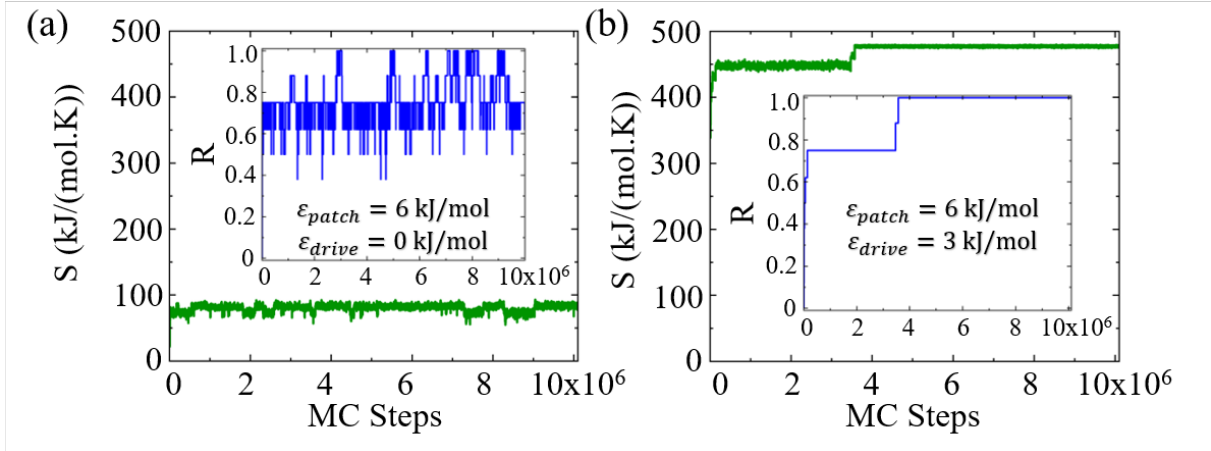


Figure S3: Total entropy production (S) as a function of MC steps (a) in equilibrium and (b) under nonequilibrium conditions with an external drive = 3 kJ/mol. Results are presented for a single MC realization of 8 particle system with $\epsilon_{patch} = 3$ kJ/mol. The insets show the variation of R .

9 Å used for our main analysis, we include additional simulations for a 15 Å and 25 Å cell, for the 10 patchy particle system (Fig. S5). Compared to simulation cells of 9 Å and 15 Å, the values of T_{fas} from both equilibrium and nonequilibrium simulations exhibit higher optimal values in the larger system due to the reduced number density, which leads to less frequent interactions among the patchy particles. Importantly, both T_{fas} and T_{stable} show the same trend in equilibrium and nonequilibrium conditions, further affirming the robustness of our conclusions, which are independent of the simulation cell dimension.

S5 Order Parameter R in Nonequilibrium Molecular Dynamics

The influence of the nonequilibrium driving forces on the self-assembly of patchy particles manifested by the order parameter R is studied for 8 and 10 patchy particle systems in equilibrium and nonequilibrium MD simulations. The average order parameter along a realization serves as an indicator of the structural alignment of the system with the desired target assembly. For the 8 particle (Fig. S6(a)-(c)) and 10 particle (Fig. S6(d)-(f)) systems,

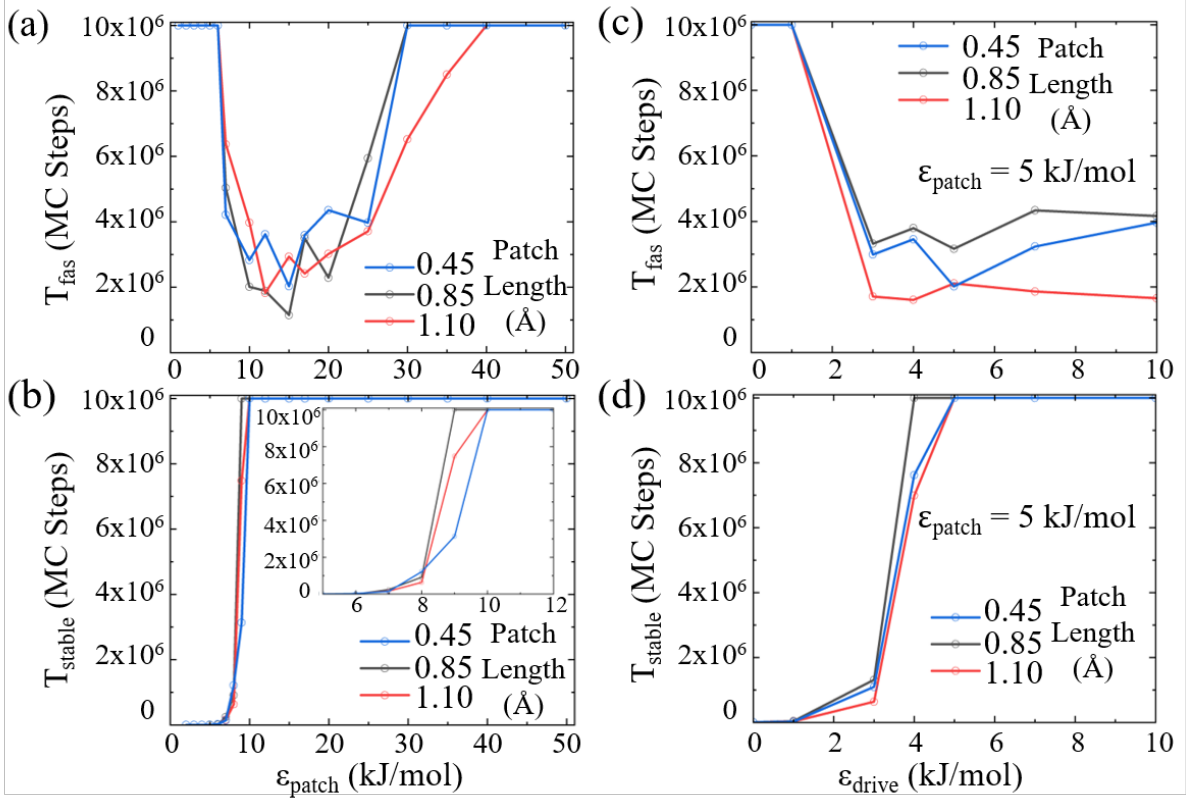


Figure S4: MC simulation results of the 10 patchy particle system from 20 independent realizations for patch lengths of 0.4 Å (blue), 0.85 Å (black), and 1.1 Å (red). (a) Median T_{fas} is plotted for different patchy particle interaction energies, ϵ_{patch} , under equilibrium conditions. (b) Median T_{stable} is plotted for different patchy particle interaction energies, ϵ_{patch} , under equilibrium conditions. Inset: Zoom into the lower ϵ_{patch} range. (c) Median T_{fas} is plotted for $\epsilon_{patch} = 5$ kJ/mol, as a function of the drive value, ϵ_{drive} , under nonequilibrium conditions. (d) Median T_{stable} is plotted for $\epsilon_{patch} = 5$ kJ/mol, as a function of the drive value, ϵ_{drive} , under nonequilibrium conditions.

we see a moderate increase in the average R value with increasing amplitude of the square wave potential, for ϵ_{patch} values of 4.5 kJ/mol, 5 kJ/mol, and 6 kJ/mol, mirroring the increase in target stability observed in Figs. 9.

S6 Bond Statistics from MD Simulation

To investigate the impact of the square wave potential, $U_{square}(t)$, on the assembly kinetics and stability, we track bond formation and dissociation events up to the point of achieving the

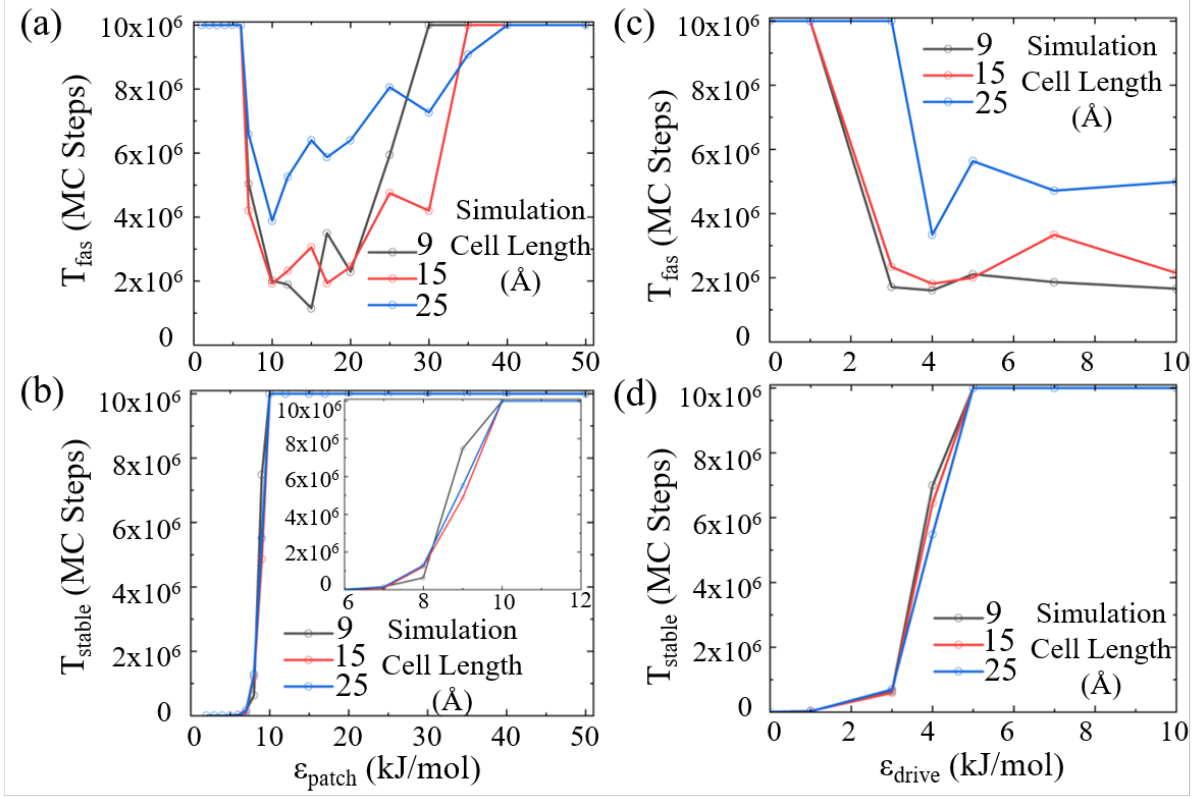


Figure S5: MC simulation results of the 10 patchy particle system from 20 independent realizations for different simulation cell dimensions of 9 Å (black), 15 Å (red), and 25 Å (blue). (a) Median T_{fas} is plotted for different patchy particle interaction energies, ϵ_{patch} , under equilibrium conditions. (b) Median T_{stable} is plotted for different patchy particle interaction energies, ϵ_{patch} , under equilibrium conditions. Inset: Zoom into the lower ϵ_{patch} range. (c) Median T_{fas} is plotted for $\epsilon_{patch} = 5$ kJ/mol, as a function of the drive value, ϵ_{drive} , under nonequilibrium conditions. (d) Median T_{stable} is plotted for $\epsilon_{patch} = 5$ kJ/mol, as a function of the drive value, ϵ_{drive} , under nonequilibrium conditions.

target structure within our nonequilibrium MD simulations, during both the high energy and low energy phases of the square wave potential. Note that for a zero amplitude, the system is effectively at equilibrium, and the bond events are averaged over the entire simulation duration and divided by two, for a fair comparison with the nonequilibrium cases in which the events are counted separately for the two potential values.

Figs. S7(a) and S7(b) present the average number of bond formation events for the 8 particle and 10 particle systems, for a patchy interaction energy of 6 kJ/mol and 5 kJ/mol, respectively. At 0 amplitude, the average number of bonds formed is ~ 3.8 for the 8 patchy

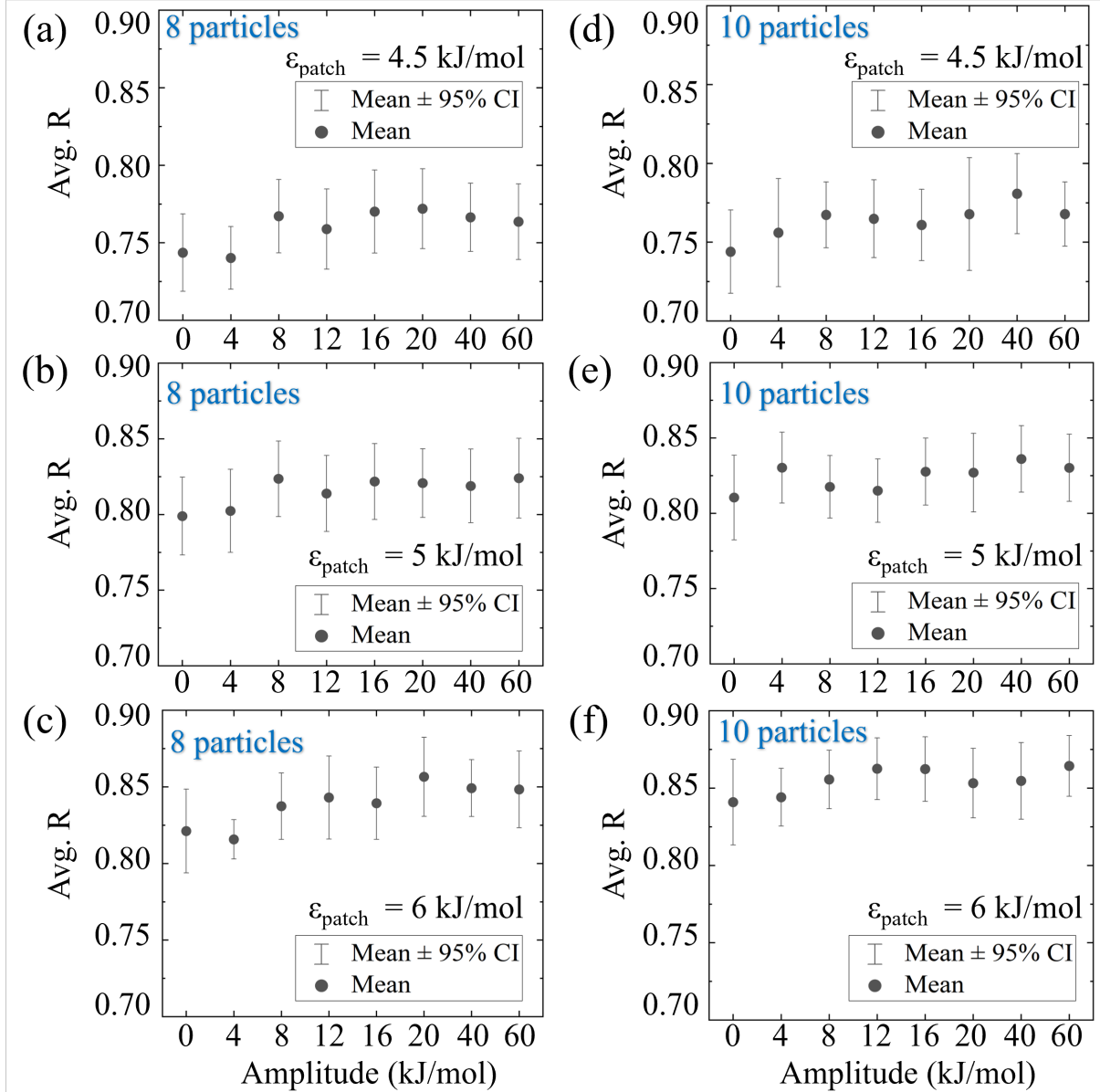


Figure S6: Average order parameter, R , from 20 different MD simulations, as a function of the square wave potential amplitude for 8 particle system and ϵ_{patch} value of (a) 4.5 kJ/mol, (b) 5 kJ/mol, and (c) 6 kJ/mol. Average order parameter, R , from 20 different MD simulations, as a function of the square wave potential amplitude for 10 particle system and ϵ_{patch} value of (d) 4.5 kJ/mol, (e) 5 kJ/mol, and (f) 6 kJ/mol.

particle system and 5.5 for the 10 patchy particle system. As the amplitude increases, the number of bond formations tends to oscillate around this equilibrium value with a significant increase in the standard deviation with respect to equilibrium.

Our analysis indicates that at 0 amplitude, the average number of bonds formed is ~ 3.8

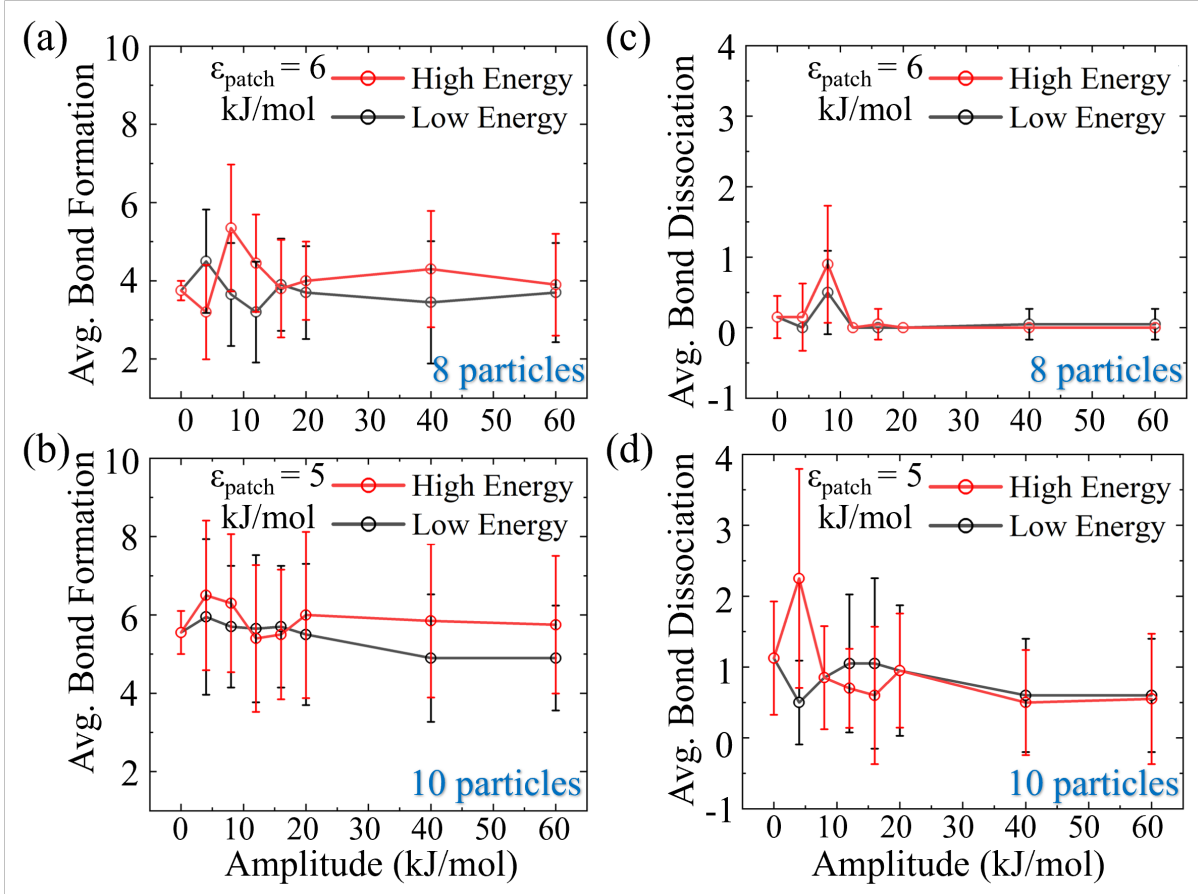


Figure S7: Average number of bond formation events across 20 individual MD simulations during the high energy (red) and low energy (black) phases of the square wave potential, as a function of its amplitude for (a) 8 patchy particles and (b) 10 patchy particles. Similar variations are shown for bond dissociation for (c) 8 patchy particles and (c) 10 patchy particles. The average number of bond dissociation events across 20 individual simulations for (a) 8 patchy particles and (b) 10 patchy particles. Error bars are standard deviations.

for the 8 patchy particle system and 5.5 for the 10 patchy particle system. As the amplitude increases, the number of bond formations tends to oscillate around this equilibrium value with a significant increase in the value of standard deviation with respect to equilibrium. Furthermore, the standard deviation bars for bond formation in the top phase overlap those in the bottom phase, suggesting that while bond formation may appear more frequent in the top phase, the difference is not statistically significant.

In terms of bond dissociation for the 8 patchy particles (Fig. S7(c)), and 10 patchy particles (Fig. S7(d)), the average bond dissociation increases from 0.15 to approximately 0.7

with increasing drive amplitude from 0 up to 8 kJ/mol for 8 patchy particles, whereas for the 10 patchy particle system the average bond dissociation increases from 1.125 to 2.25 for the high energy phase for drive amplitude value of 4 kJ/mol. Beyond these amplitudes, the average bond dissociation reduces to approximately 0 for the 8 patchy particles and approximately 0.55 for the 10 patchy particle system, and the corresponding standard deviations fall below their equilibrium values.

This observation suggests that up to a certain value of drive amplitude, the bond-breaking events increase, whereas, for larger amplitudes, fewer bonds are broken relative to the equilibrium conditions. Therefore, the overall durability of bonds in our patchy particle system increases in response to the increase in the square wave amplitudes, thereby increasing target stability and facilitating target assembly, as seen in Fig. 11 of the main text.

S7 Self-Assembly of Large Systems in the Presence of External Drive

To demonstrate the efficacy of our proposed design principle of employing nonequilibrium force in overcoming equilibrium limitations for larger systems, we present here the equilibrium and nonequilibrium simulations of 100 patchy particles, with patches modeled to form 8 and 4 sided rings. It should be noted that since each particle has two patches and each patch forms one bond, the total number of bonds formed in the system of 100 particles would be 200.

Fig. S8 illustrates the variation of the number of bonds (N_B) as a function of MC steps, highlighting the impact of ϵ_{patch} and ϵ_{drive} . In Fig. S8(a), N_B is plotted for different values of ϵ_{patch} in equilibrium. The results show that higher values of ϵ_{patch} lead to an increased number of bonds, with the number rapidly rising before plateauing at 200. This indicates that stronger interaction energies promote more stable and numerous bond formations. Fig. S8(b) presents N_B for varying ϵ_{drive} . It shows that applying an external drive increases N_B to 200

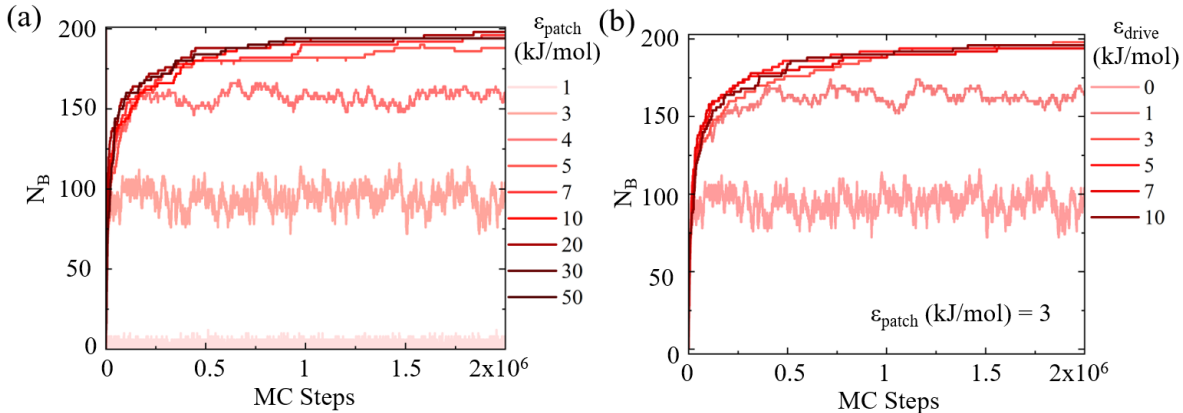


Figure S8: Variation of N_B as a function of MC Steps for (a) different values of interaction energy between patches (ϵ_{patch}) in equilibrium and (b) different values of external drive (ϵ_{drive}) for patchy interaction energy of 3 kJ/mol from single realizations. Two patches are separated from each other by an angular difference of 135° (interior angle of the octagon).

while keeping ϵ_{patch} constant at 3 kJ/mol. In equilibrium, the number of bonds formed with the same ϵ_{patch} value (3 kJ/mol) fluctuates around ~ 100 . The findings, therefore, reveal that increasing ϵ_{drive} leads to a higher number of bonds for weak ϵ_{patch} , suggesting that the external drive enhances bond formation beyond equilibrium conditions similar to our earlier observation for small systems. In this system, throughout the equilibrium and nonequilibrium conditions, the resultant structure has the shape of a chain with very infrequent formation of large ring structures of ~ 20 -sides (see Movie S11).

Fig. S9 illustrates the variation in N_B and the number of ring structures (N_R) as a function of MC steps, with a focus on the impact of the interaction energy between patches and external drives on bond and ring formation. Figs. S9(a) and S9(b) display N_B for different values of interaction energy ϵ_{patch} in equilibrium and different values of ϵ_{drive} , respectively. In Fig. 5, we identified three regions of T_{fas} variation with different ϵ_{patch} values. In the scenario of a large system, T_{fas} represents the MC step when all the particles form bonds with each other. In Figs. S8(a) and S9(a), we observe Regions I and II in a larger system: Region I (low ϵ_{patch} , low N_B) and Region II (increasing ϵ_{patch} , N_B approaching 200). However, Region III is absent in the larger system due to increased particle interactions and mobility, leading to

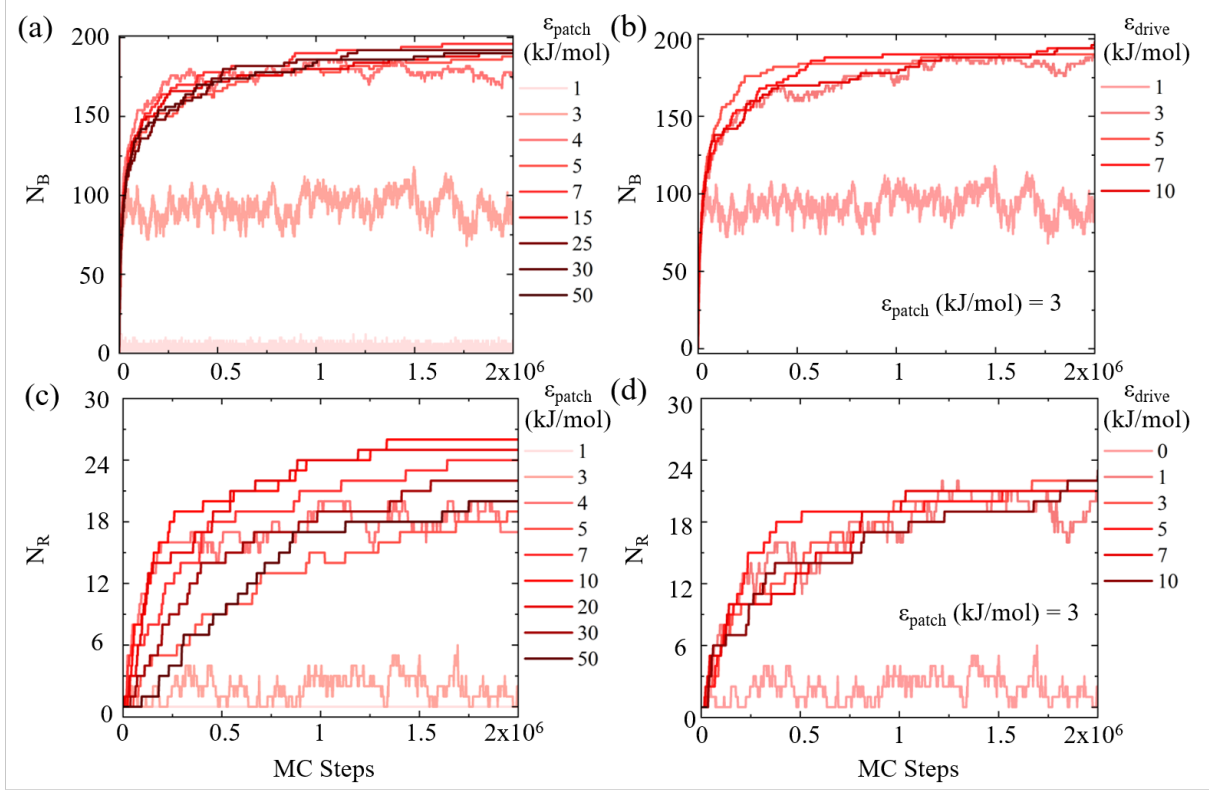


Figure S9: Variation of N_B as a function of MC Steps for (a) different values of interaction energy between patches in equilibrium and (b) different values of external drive for patchy interaction energy of 3 kJ/mol from single realizations. Variation of N_R as a function of MC Steps for (c) different values of interaction energy between patches in equilibrium and (d) different values of external drive for patchy interaction energy of 3 kJ/mol from single realizations. Two patches are separated from each other by an angular difference of 90° (interior angle of a square).

diverse structures like rings and chains and preventing a high-energy overbound state. Thus, the larger system only exhibits Regions I and II, reflecting either no structure formation or stable ring and chain formations.

The results are similar to what we observed in Fig. S8. In this system, we observed the formation of a ring structure comprising mainly 4 and 5 particles with the infrequent occurrence of a large polygon of 9 or 10 sides (see Movie S12). Figs. S9(c) and S9(d) present N_R , for varying ϵ_{patch} and then for different ϵ_{drive} for a specific patch interaction energy of 3 kJ/mol, respectively. Here, we observe that an increase in values of ϵ_{patch} resulted in more ring formation (Region II) compared to weak ϵ_{patch} (Region I), with a significant observation

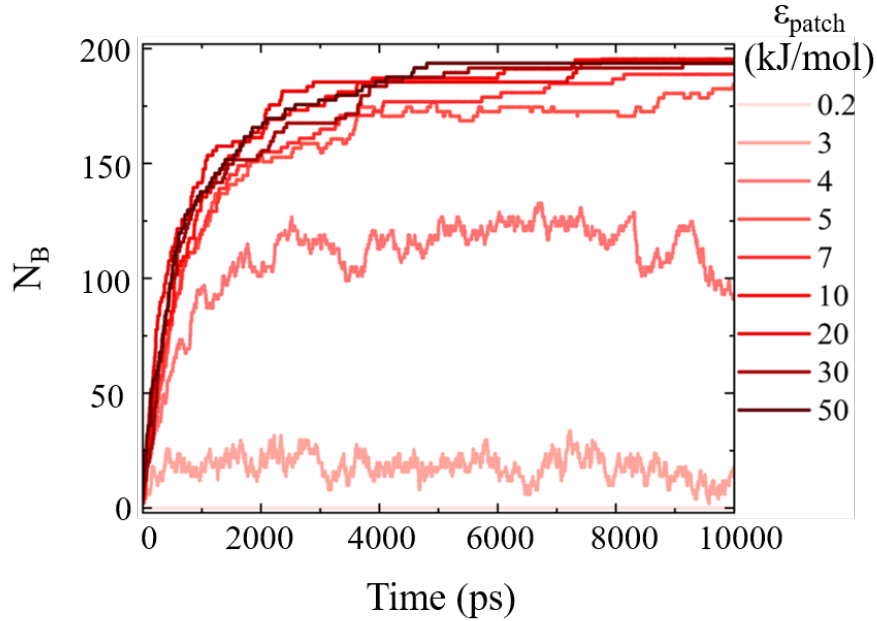


Figure S10: Variation of N_B as a function of time for different values of the interaction energy between patches obtained from equilibrium MD simulations. Two patches are separated from each other by an angular difference of 90° (interior angle of a square).

of a lower number of ring formations for higher ϵ_{patch} value akin to region III of Fig. 5 of the main manuscript. Application of ϵ_{drive} results in a higher number of ring formations compared to equilibrium conditions.

Fig. S10 illustrates the variation in N_B as a function of time for different values of ϵ_{patch} , obtained from equilibrium MD simulations. In this case, the patches are separated by an angular difference of 90 degrees (interior angle of a square). The plot shows that for lower ϵ_{patch} values, N_B fluctuates around small values indicating that only a few bonds were formed, where more bonds formed over time with increasing ϵ_{patch} values. Higher values of ϵ_{patch} lead to a greater maximum N_B (200 for the system of 100 particles) and a higher stabilization plateau, indicating more extensive bond formation. Specifically, $\epsilon_{patch} = 50$ kJ/mol results in the highest number of stable bonds, while $\epsilon_{patch} = 0.2$ kJ/mol shows the lowest. This trend is similar to what we observed from Fig. S9(a) for the same system simulated using MC. This result confirms that the observed qualitative behaviors are consistent across both methods and are intrinsic to the assembly process.

S8 Supplementary movies

Movie S1: Equilibrium MC simulation of 8 patchy particles, with 2 internal states, contained within a cubic box of 8 Å side length with reflective boundaries. The simulation employs an interaction energy of 3 kJ/mol for interactions between patches and does not incorporate any external driving forces. Conducted at a temperature of 65 K, the simulation spans 10×10^6 MC steps, with the trajectory recorded every 1000th step.

Movie S2: Equilibrium MC simulation of 10 patchy particles, with 2 internal states, confined within a cubic box of 9 Å in length and featuring reflective boundaries. The simulation utilizes an interaction energy of 3 kJ/mol among the patches, with no external driving forces applied. It is conducted at a temperature of 65 K over 10×10^6 MC steps, with the trajectory being captured every 1000th MC step.

Movie S3: Equilibrium MC simulation of 13 patchy particles with 2 internal states, within a cubic box of 15 Å in length. The simulation is executed with an interaction energy of 4 kJ/mol between the patches in the absence of an external driving force. Conducted at 65 K, the simulation proceeds for 15×10^6 MC steps, with trajectory data recorded every 1000th step.

Movie S4: Nonequilibrium MC simulation of 8 patchy particles, with 2 internal states, contained within a cubic box of 48 Å side length and reflective boundaries. This simulation is executed with an interaction energy of 3 kJ/mol between the patches, under the influence of an external driving force of 7 kJ/mol. Performed at a temperature of 65 K, the simulation extends over 10×10^6 MC steps, with the trajectory being recorded every 1000th step.

Movie S5: Nonequilibrium MC simulation of 10 patchy particles, with 2 internal states, enclosed in a cubic box of 9 Å side length with reflective boundaries. The simulation utilizes an interaction energy of 3 kJ/mol between patches, alongside an external driving force of 7 kJ/mol. Conducted at 65 K, the simulation proceeds for 10×10^6 MC steps, with trajectory data recorded every 1000th step.

Movie S6: Nonequilibrium MC simulation of 13 patchy particles with 2 internal states,

within a cubic box of 15 Å in length. The simulation is executed with an interaction energy of 4 kJ/mol between the patches in the presence of an external driving force of 7 kJ/mol. Conducted at 65 K, the simulation proceeds for 15×10^6 MC steps, with trajectory data recorded every 1000th step.

Movie S7: Equilibrium MD simulation of 8 patchy particles with 1 internal state within a cubic box of 8 Å in length with periodic boundaries. The simulation is executed with an interaction energy of 4.5 kJ/mol between the patches. It is performed at 40 K for 12000 ps, with the trajectory being recorded every 2 ps.

Movie S8: Equilibrium MD simulation of 10 patchy particles with 1 internal state within a cubic box of 9 Å in length with periodic boundaries. The simulation is executed with an interaction energy of 5 kJ/mol between the patches. It is performed at 40 K for 12000 ps, with the trajectory being recorded every 2 ps.

Movie S9: Nonequilibrium MD simulation of 8 patchy particles with 1 internal state within a cubic box of 8 Å in length with periodic boundaries. The simulation is executed with an interaction energy of 4.5 kJ/mol between the patches with a square wave potential with an amplitude of 20 kJ/mol. It is performed at 40 K for 12000 ps, with the trajectory being recorded every 2 ps.

Movie S10: This movie demonstrates a nonequilibrium MD simulation of 10 patchy particles with 1 internal state within a cubic box of 9 Å in length with periodic boundaries. The simulation is executed with an interaction energy of 5 kJ/mol between the patches with a square wave potential with an amplitude of 12 kJ/mol. It is performed at 40 K for 12000 ps, with the trajectory being recorded every 2 ps.

Movie S11: This movie presents an equilibrium MC simulation of 100 patchy particles with patches of 8-ring specification, with 1 internal state, contained within a cubic box of 30 Å side length with periodic boundaries. The simulation employs an interaction energy of 20 kJ/mol for interactions between patches and does not incorporate any external driving forces. Conducted at a temperature of 40 K, the simulation spans 2×10^6 MC steps, with

the trajectory being recorded every 1000th step.

Movie S12: This movie presents an equilibrium MC simulation of 100 patchy particles with patches of 4-ring specification, with 1 internal state, contained within a cubic box of 30 Å side length with periodic boundaries. The simulation employs an interaction energy of 20 kJ/mol for interactions between patches and does not incorporate any external driving forces. Conducted at a temperature of 40 K, the simulation spans 2×10^6 MC steps, with the trajectory being recorded every 1000th step.

References

- (1) Bisker, G.; Polettini, M.; Gingrich, T. R.; Horowitz, J. M. Hierarchical bounds on entropy production inferred from partial information. *Journal of Statistical Mechanics: Theory and Experiment* 2017, 093210.